

# ***Toxoplasma* scavenges mammalian host organelles through the usurpation of host ESCRT-III and Vps4**

Julia D. Romano<sup>1,\*</sup>, Joshua Mayoral<sup>2</sup>, Rebekah B. Guevara<sup>2</sup>, Yolanda Rivera-Cuevas<sup>3</sup>,  
Vern B. Carruthers<sup>3</sup>, Louis M. Weiss<sup>2,4</sup>, and Isabelle Coppens<sup>1,\*</sup>

<sup>1</sup>Department of Molecular Microbiology and Immunology, Johns Hopkins University Bloomberg School of Public Health, Baltimore, MD, 21205, USA

<sup>2</sup>Department of Pathology, Albert Einstein College of Medicine, Bronx, NY, 10461, USA

<sup>3</sup>Department of Microbiology and Immunology, University of Michigan Medical School, Ann Arbor, MI, 48109, USA

<sup>4</sup>Department of Pathology Medicine, Albert Einstein College of Medicine, Bronx, NY, 10461, USA

\*Corresponding authors:

icoppens@jhspsh.edu; 443-287-1589

jromano2@jhu.edu; 443-287-1588

ORCID IDs: 0000-0001-5549-2362 (IC); 0000-0001-8956-7377 (JDR); 0000-0003-0859-2226 (JM);  
0000-0002-8040-3453 (RBG); 0000-0001-8389-5724 (YCR); 0000-0001-6859-8895 (VBC); 0000-0002-  
0357-7396 (LMW)

## **Summary**

The parasite *Toxoplasma* sequesters host nutrient-filled organelles into its parasitophorous vacuole through its exploitation of host ESCRT-III and Vps4 for vacuolar membrane-remodeling and fission processes utilizing the parasite proteins TgGRA14 and TgGRA64 that interact with ESCRT.

## **Abstract**

Intracellular pathogens exploit cellular resources through host cell manipulation. Within its nonfusogenic parasitophorous vacuole (PV), *Toxoplasma* targets host nutrient-filled organelles and sequesters them into the PV through deep invaginations of the PV membrane (PVM) that ultimately detach from this membrane. Some of these invaginations are generated by an intravacuolar network (IVN) of parasite-derived tubules attached to the PVM. Here, we examine the parasite usurpation of host ESCRT-III and Vps4 to create PVM buds and vesicles. CHMP4B associates with the PVM/IVN and dominant negative (DN) CHMP4B forms many long PVM invaginations containing CHMP4B filaments; the invaginations are shorter in IVN-deficient parasites, suggesting cooperation between IVN and ESCRT. In infected cells

expressing Vps4-DN, enlarged intra-PV structures containing host endo-lysosomes accumulate, reflecting defects in PVM scission. Parasite mutants lacking TgGRA14 or TgGRA64 that interact with ESCRT have reduced CHMP4B-DN-induced PVM invaginations and intra-PV host organelles, with greater defects in a double-knockout, revealing the exploitation of ESCRT to scavenge host organelles by *Toxoplasma*.

## Introduction

Biotrophic microbes adapt to life inside host cells by evading host responses to infection and by exploiting surrounding resources to promote multiplication. The apicomplexan protozoan *Toxoplasma gondii* is an obligate intracellular parasite that invades mammalian cells and creates its own replicative niche, the parasitophorous vacuole (PV) in the host cell cytoplasm. One critical factor of the success of *Toxoplasma* post-invasion (p.i.) is the secretion of unique proteins from parasite dense granule organelles that transform the PV into a replicative niche and modify the host cell. These proteins, usually named “GRAs” (64, so far) exert broad functions ranging from nutrient uptake, host organelle attraction, and protein export from the PV into the host cell to control cellular signaling pathways, in particular those involved in innate immune responses and cell cycle (reviewed in (Mercier and Cesbron-Delauw, 2015; Panas and Boothroyd, 2021; Griffith et al., 2022)).

Within *Toxoplasma*-infected cells, many cellular structures are reorganized and intercepted by the parasite. The host microtubular network is rearranged around the PV, allowing host organelles translocating along microtubules to cluster near the PV. Some microtubules create invaginations of the PVM in which host organelles are engulfed (Coppens et al., 2006). Inside the PV, membranous tubules secreted by the parasite form an intravacuolar network (IVN) stabilized by two tubulogenic proteins, TgGRA2 and TgGRA6 (Sibley et al., 1995; Mercier et al., 2002; Bittame et al., 2015). Some IVN tubules connect to the PVM (de Souza and Attias, 2015; Magno et al., 2005) and form open conduits entrapping host organelles, resulting in their sequestration into the PV (Coppens et al., 2006; Romano et al., 2017; Hartman et al., 2022); *Toxoplasma* mutants with a defective IVN ( $\Delta gra2$  and  $\Delta gra2\Delta gra6$ ) have a reduced number of intra-PV host organelles. *Toxoplasma* secretes a phospholipase TgLCAT into the PV that localizes to IVN membranes surrounding internalized host organelles and destabilizes membranes by producing lysophospholipids from the release of fatty acids from phospholipids (Pszenny et al., 2016).

We have observed that host organelles, initially trapped in PVM invaginations, accumulate in the PV center, suggesting dissociation from the PVM (Romano et al., 2017). Tubule detachment from the PVM may be analogous to the biogenesis of intraluminal vesicles (ILV) from budded portions of the limiting membrane of multivesicular bodies (MVB), mediated by Endosomal Sorting Complex Required for Transport (ESCRT) components, with the ESCRT-III complex and the associated AAA-ATPase Vps4 responsible for membrane scission (Piper and Katzmann, 2007; Schöneberg et al., 2017). The core

ESCRT machinery can be subdivided into distinct subcomplexes (ESCRT-I, ESCRT-II, ESCRT-III) and accessory proteins, e.g., apoptosis linked gene 2 (ALG-2, also known as PDCD6) and ALG-2-interacting protein X (ALIX) (Vietri et al., 2020; Schöneberg et al., 2017). ESCRT-III directly reshapes and severs membranes in conjunction with Vps4 while the other subcomplexes and accessory proteins are involved in targeting and activating ESCRT-III (Vietri et al., 2020; Schöneberg et al., 2017; Pfitzner et al., 2021). ESCRT-III is composed of oligomers of Charged Multivesicular Body Protein (CHMP), e.g., CHMP2A/B, CHMP3, CHMP4A/B, with CHMP4 as the most abundant component (Teis et al., 2008; Schöneberg et al., 2017; Vietri et al., 2020). Through an auto-inhibition domain, CHMP proteins form inactive monomers in the cytosol, and upon release of auto-inhibition, activated CHMP proteins polymerize into filaments on membranes and adopt a variety of secondary shapes, resulting in membrane remodeling and scission (Alonso Y Adell et al., 2016; Cashikar et al., 2014; Harker-Kirschneck et al., 2019).

Association of host ESCRT components with the PV of *Toxoplasma* has recently become an active area of research. *Toxoplasma* recruits and utilizes host ALIX and tumor susceptibility gene 101 protein (TSG101) from ESCRT-I during parasite invasion (Guérin et al., 2017). A proximity-labeling study on *Toxoplasma*-infected fibroblasts to identify host proteins at the PV, reveals that a PVM reporter biotinylates several host ESCRT components (e.g., ALIX, ALG-2, TSG101, VPS28, CHMP4B, CC2D1A) (Cygan et al., 2021). Two concomitant studies using co-immunoprecipitation and proximity-based biotinylation identified two *Toxoplasma* proteins on the PVM/IVN that interact with host ESCRT: TgGRA14 (e.g., ALIX, ALG-2, TSG101, CHMP4A/B) (Rivera-Cuevas et al., 2021) and TgGRA64 (e.g., TSG101, VPS37A, VPS28, CHMP4B, ALG-2) (Mayoral et al., 2022). Some of these host ESCRT components have been shown to associate with the PV; ALIX and ALG-2 localize as puncta on the PV (Cygan et al., 2021) and TgGRA14 influences PV recruitment of TSG101 (Rivera-Cuevas et al., 2021). The uptake of host cytosolic proteins by *Toxoplasma* (Dou et al., 2014) is reduced in mammalian cells ectopically expressing the Vps4A EQ dominant negative (DN) mutant or by  $\Delta gra14$  mutant parasites (Rivera-Cuevas et al., 2021).

We hypothesize that host ESCRT machinery diverted by *Toxoplasma* is involved in the scission of IVN tubules containing host vesicles from the PVM. In this study, we analyzed by fluorescence microscopy and transmission EM (TEM) the recruitment of the ESCRT-III component CHMP4B and Vps4 to the PV to assess their impact on PVM remodeling for host organelle internalization. We also examined the distribution of several host ESCRT components on the IVN where intra-PV host organelles accumulate. Finally, we compared the ability of wild-type (WT) and mutants lacking *gra14* and/or *gra64* to scavenge host Rab11 vesicles.

## Results

### Endogenous ESCRT-III component CHMP4B is recruited to the *Toxoplasma* PV

A principle target of intravacuolar *Toxoplasma* is the endosomal recycling pathway in the host mammalian cell (Romano et al., 2017; Hartman et al., 2022). Rab11A localizes to the endocytic recycling compartment (ERC)/recycling endosome and trans-Golgi network to regulate vesicular trafficking between these compartments (Maxfield and McGraw, 2004). Endogenous Rab11A in uninfected cells localized as puncta throughout the cytoplasm with a concentration near the nucleus where the ERC is predominantly located (Fig. 1 A). In *Toxoplasma*-infected cells, the PV localizes near the host ERC and Rab11A-positive vesicles. *Toxoplasma* internalizes host GFP-Rab11A vesicles into the PV (89%) using IVN tubules appended to the PVM, creating conduits into the PV (Coppens et al., 2006; Romano et al., 2017). We detected several endogenous Rab11A foci on IVN patches (TgGRA7) (Fig. 1A), as previously reported (Romano et al., 2017). The exploitation of IVN tubules to sequester host organelles was further confirmed by TEM of infected cells incubated with LDL-gold particles to track host endo-lysosomes. Data illustrate IVN tubules attached to the PVM (Fig. 1 B, panel a), with some containing LDL-containing organelles in the process of penetrating into a tubule lumen (Fig. 1 B, panel b) or inside a tubule distant from the PVM (Fig. 1 B, panel c), suggesting scission from the PVM. To examine whether host ESCRT machinery is recruited by *Toxoplasma* to induce PVM buds and long invaginations into the PV lumen to facilitate host organelle internalization via the IVN, we monitored the distribution of CHMP4B upon *Toxoplasma* infection. HeLa cells stably expressing GFP-CHMP4B (Jouvenet et al., 2011) were infected for 6 h or 24 h to compare with uninfected cells. GFP-CHMP4B was detected in the nucleus and the cytoplasm, in addition to some defined vesicles in uninfected HeLa cells (Fig. 1 C, panel a); this specific localization was confirmed by silencing of GFP-CHMP4B (Fig. S1 A). In infected cells for 6 h, the staining for GFP-CHMP4B was observed around the PV (Fig. 1C, panel b) and often as well-defined puncta along the edge of the PVM (identified with antibodies against TgGRA7) (Fig. 1 C, panel c). At 24 h post-infection (p.i.), the GFP-CHMP4B signal was more prominent on several area of the PVM and patches of the IVN (Fig. 1 C, panels d and e), suggesting CHMP4B recruitment. Measurements of Mander's colocalization coefficients (MCC) suggest a correlation between the GFP-CHMP4B and TgGRA7 (PVM/IVN) signals. To examine the role of the IVN in CHMP4B internalization into the PV, we monitored GFP-CHMP4B in HeLa cells infected with the  $\Delta gra2\Delta gra6$  mutant that has a defective IVN (Mercier et al., 2002) and is deficient in host vesicle internalization (Romano et al., 2017). GFP-CHMP4B puncta were observed along the  $\Delta gra2\Delta gra6$  PV periphery, with few puncta detected in the PV lumen (Fig. 1 C, panel f). We assessed the intra-PV distribution of host GFP-CHMP4B relative to PV-associated Rab11A vesicles; an accumulation of GFP-CHMP4B and Rab11A puncta along the edge of the PV (Fig. S1 B, panel a) with a partial overlap of a few puncta was observed (Fig. S1 B, panel b),

suggesting a possible involvement of CHMP4B in host vesicle internalization into the PV in synergy with IVN tubules.

### **Dominant negative CHMP4B tagged with mEmerald at the N- or C-terminus is targeted to different locations at the PV**

Host CHMP4B partially localizes to the PVM and the IVN, supporting the hypothesis that *T. gondii* utilizes the host ESCRT-III complex during infection. CHMP4B undergoes a conformation change that exposes C-terminal domains to recruit Vps4 and other effectors, such as ALIX, enabling membrane binding, oligomerization, and scission (Tang et al., 2015; Muziol et al., 2006; Lata et al., 2008; Obita et al., 2007; McCullough et al., 2008; Henne et al., 2012; Lin et al., 2005). Ectopic expression of CHMP proteins with bulky protein tags on either the N- or C-terminus may interfere with conformational changes and cause DN effects leading to the formation of enlarged endosomal “class E-like” compartments (Martin-Serrano et al., 2003; Howard et al., 2001; von Schwedler et al., 2003). Taking advantage of the DN effect that ESCRT-III subunits tagged with large fluorophores have on complex activity, we investigated the DN effect of CHMP4B on the PV. We overexpressed CHMP4B tagged with mEmerald either at the N- (mEm-CHMP4B) or C- (CHMP4B-mEm) terminus in HeLa cells. In uninfected cells expressing either construct, large punctate structures consistent with enlarged “class E” compartments containing tagged CHMP4B were observed throughout the cytoplasm (Fig. 2 A and B). In cells expressing mEm-CHMP4B and infected with WT parasites for 20 h, mammalian “class E” compartments surrounded the PV and discrete mEm-CHMP4B puncta were detected on the PVM and inside the PV within IVN patches (Fig. 2 A, Fig. S2 A). In cells infected with the IVN mutant  $\Delta gra2\Delta gra6$ , mEm-CHMP4B compartments associated with the PV but no puncta were observed within; faint mEm-CHMP4B staining was observed along the PVM (Fig. 2 A). In contrast, in infected cells expressing CHMP4B-mEmerald, the signal was predominantly distributed on the PVM of both WT and  $\Delta gra2\Delta gra6$  parasites, and no puncta were observed within the PV (Fig. 2 B, Fig. S2 B).

Next, we monitored CHMP4B-mEm recruitment at the PV over time by measuring colocalization of CHMP4B-mEm and TgGRA7 at the PVM using the Mander’s colocalization coefficient (MCC). We observed that CHMP4B-mEm progressively associated with the PVM (Fig. S2 C), with a mean MCC value for TgGRA7 of 0.232 at 20 min p.i. and increasing to 0.716 at 8 h p.i. (a time point typically corresponding to the first round of *Toxoplasma* division) (Fig. 2 C, Fig. S2 C). The mean MCC values for CHMP4B-mEm also trended higher as the infection progresses (Fig. S2 C and D). Late in infection (40 h p.i.) prior to *Toxoplasma* egress, CHMP4B-mEm staining was mainly detected on the PVM, suggesting continuous recruitment by the parasite (Fig. 2 D). Interestingly, CHMP4B association with the PV occurred even when the bulk of CHMP4B-mEm localized far from the PV, e.g., on the other side of the

host nucleus (Fig. 2 E) and was also observed along projections of the PVM that extend into the host cytosol (Fig. S2 C, 8 h p.i.).

To scrutinize the association of mEmerald-tagged CHMP4B with the PVM in finer detail, we performed immuno-EM using anti-GFP antibodies on infected cells expressing either construct. Within the mammalian cell, gold particles localized mEm-CHMP4B and CHMP4B-mEm to multilamellar “class E” compartments (Fig. 2 F). In infected cells, PV-associated mEm-CHMP4B predominantly distributed to IVN tubules while gold particles detecting CHMP4B-mEm were observed aligned along the PVM, covering the PV entirely on each cryosection. Altogether, these observations highlight that after induction of DN CHMP4B in infected cells, *Toxoplasma* actively recruits CHMP4B to the PV, but the final destination of this protein on the PV differs according to the mEmerald tag position. mEm-CHMP4B is internalized into the PV while CHMP4B-mEm is trapped in this membrane, which suggests that the C-terminal mEmerald tag allows PVM recruitment of CHMP4B but interferes with later scission steps from this membrane.

### **The PVM containing host CHMP4B-mEmerald invaginates and buds into the PV lumen**

We examined in greater detail and resolution the ultrastructure of the massive recruitment of CHMP4B-mEm at the PVM in ultra-thin resin embedded cells. In non-transfected cells, the PVM had a relatively flat appearance with closely apposed host mitochondria and ER elements (Fig. 3 A, panel a). These host organelles form intimate association with the PVM mediated by parasite proteins (Melo et al., 1992; Melo and Souza, 1997; Sinai et al., 1997; Pernas and Boothroyd, 2010; Pernas et al., 2014) but are never detected within the PV, unlike host endocytic organelles. Higher magnification observations reveal PVM indentations containing host LDL-containing organelles, seemingly targeted by tubules of the IVN as a point of anchorage and fusion for host organelle internalization into the PV (Fig. 3 A, panel b). Infected cells transfected with CHMP4B-mEm were identified by the presence of “class E” compartments in the host cytosol. Unlike PV in non-transfected cells, the PVM containing CHMP4B-mEm displayed a corrugated morphology, with tubular (up to 450 nm-long) and numerous invaginations (often spaced less than ~50 nm spaced from each other) detected over the entire surface of this membrane (Fig. 3 B). In transfected cells expressing CHMP4B-mEm and infected with  $\Delta gra2\Delta gra6$  parasites, the PVM also contained CHMP4B-mEm, though to a lesser extent than WT PVM (Fig. 1 C), and underwent the same deformation process with the generation of nanosized buds away from the host cytoplasm (Fig. 3 C). However, the PVM buds in the  $\Delta gra2\Delta gra6$  mutant were rarer, further apart, and smaller in size (~80 nm long), suggesting IVN tubules may contribute to supply membranes at PVM bud sites in WT PV.



Replicating *Toxoplasma* usually distribute radially, forming a rosette-like structure inside the PV. However, upon CHMP4B-mEm recruitment, the parasites were often spatially disorganized within the PV, with very little recruitment of host mitochondria and ER at the PVM (Fig. S3 A). Furthermore, some PV dually stained for CHMP4B and TgGRA7 appear ‘empty’, a sign of *Toxoplasma* deterioration (Fig. S3 B and C). In cells expressing CHMP4B-mEm, enumeration of parasites per PV at 20 h p.i. shows that ~35% of PV contained 8 parasites similarly to cells expressing mEm-CHMP4B, but uniquely ~15% of PV did not harbor any parasites (Fig. S3 D).

High magnification observations of PVM containing host CHMP4B-mEmerald reveal, on longitudinal sections of tubular invaginations, regularly displayed constrictions on a horizontal plan and continuing the length of the tubular structures, resulting in a reduction of the membrane tube radius (Fig. 3 D). The overall diameter of the PVM tubules was uniform ( $105 \pm 10$  nm). Our morphological analyses suggest sequential steps in the formation of PVM tubular invaginations. Initially, distinct filamentous structures, likely CHMP4B polymers, accumulated at many areas of the PVM. Then, these confined areas decorated with filaments evolved from flat to small buds (Fig. 3 E, panel a). Filaments were detected in the interior of the buds, organized into rings attached to membrane (Fig. 3 E, panel b). Finally, concomitant to the incorporation of filaments into PVM buds, these latter transformed progressively into long tubules up to 8  $\mu$ m that underwent constriction with decreased diameter (Fig. 3 E, panel c). Immunostaining for CHMP4B confirms the presence of gold particles coating the interior of PVM invaginations (Fig. 3 F, panel a). Stabilized ESCRT-III filaments including CHMP4B polymers, are frequently organized into spirals on curved membranes (Cashikar et al., 2014). A similar organization of CHMP4B filaments was observed within PVM tubules, as observed in a tangential section showing gold particle distribution in a spiraled pattern (S-shape) (Fig. 3 F, panel b) and on transversal sections of PVM tubules showing CHMP4B filaments (characterized by high electron-density layer beneath the tubule membrane) forming a partial ring that may reflect a spiral configuration (Fig. 3 G). We noticed that some PVM tubules appeared slightly bent (Fig. 3 D and H) and branched, with some bifurcations reminiscent of IVN tubules that may have fused with large PVM tubules containing CHMP4B filaments (Fig. 3 D and I).

Altogether these observations suggest that host CHMP4B recruited at the PVM assemble into filaments at the membrane surface, driving tubular invaginations away from the cytoplasm. Within PVM tubules, assembled CHMP4B filaments narrow the tubule, similar to the CHMP4A internal coat on negatively-curved membranes, to draw membranes together to the fission point (McCullough et al., 2015).

### **FLAG-tagged CHMP4B localizes to the PVM and as enlarged puncta within the PV close to Rab11A vesicles**

Overexpression of CHMP proteins fused to a protein tag leads to DN effects, presumably due to the bulky tag interfering with inhibitory intramolecular interactions necessary to keep CHMP proteins in an inactive soluble form. Thus, we opted to use CHMP4B tagged with a FLAG tag (8 amino acids; ~1 kDa) at the N-terminus (FLAG-CHMP4B). Previous studies reported FLAG-CHMP4B localization as a punctate pattern upon transient transfection in HeLa cells and a more diffuse cytoplasmic distribution upon stable expression in HEK293 cells, with vesicle-like structures observed in 5% of the cells (Katoh et al., 2003). We confirmed the localization of FLAG-CHMP4B as disperse puncta, partially concentrated in the perinuclear region in HeLa cells, as a result of overexpression (Fig. 4 A, panel a). In HeLa cells infected with *T. gondii* for 20 h, three patterns for FLAG-CHMP4B distribution were observed: 66% of cells displayed a FLAG-CHMP4B signal throughout the host cell with partial localization to the PV, while 34% exhibited a signal predominantly associated with the PV (Fig. 4 A, panel b). Among the 34% population, FLAG-CHMP4B was observed either as very large intra-PV puncta (up to 1  $\mu$ m in diameter) near IVN patches (23%) or all along the PVM (11%). The majority of large intra-PV puncta containing FLAG-CHMP4B had a torus shape that colocalized with TgGRA7, suggesting that CHMP4B puncta are derived from the PVM (Fig. 4 A, panel c).

We assayed if CHMP4B puncta localize in close proximity to intra-PV Rab11A puncta by infecting HeLa cells expressing FLAG-CHMP4B and immunostaining for Rab11A. Several intra-PV FLAG-CHMP4B and Rab11A puncta were detected in patches of TgGRA7 signal, presumably overlapping with the IVN, and to a lesser extent with each other (Fig. 4 B and Fig. S4 A and B). We next conducted EM observations to scrutinize the PVM in infected HeLa cells expressing FLAG-CHMP4B. In the cytoplasm of transfected cells, many vesicles of variable size were generated (Fig. S4 C). In all PV examined in transfected cells, no PVM tubulation or unusual remodeling was observed (Fig. S4 D), similar to the PV in cells expressing mEm-CHMP4B (Fig. 2 F). However, the PV lumen contained several large unique structures (up to 700 nm in diameter) composed of numerous vesicles (20 to 100 nm in diameter) encircled by membrane and close to the IVN, with some attached to the PVM (Fig. 4 C). These large multivesicular structures were reminiscent of large CHMP4B puncta surrounded by TgGRA7, detected by IFA (Fig. 4 A, panel b). Based on size and electron-density, we interpret the nature of the luminal vesicles to likely be host endosomal vesicles formed upon CHMP4B overexpression that are subsequently internalized into the PV and surrounded by the PVM.

To assess if IVN tubules could be involved in the internalization of FLAG-CHMP4B into the PV, FLAG-CHMP4B-expressing cells were infected with  $\Delta$ *gra2* $\Delta$ *gra6* parasites. Two patterns for FLAG-CHMP4B distribution in infected cells were discernible: partial staining of the PV with the bulk in the



host cytoplasm (58%) or preponderant PV labeling (42%) with no intra-PV puncta detected (Fig. 4 D), suggesting that IVN tubules are important for the accumulation of FLAG-CHMP4B in the PV.

### **Dominant negative Vps4A results in PV swelling and accumulation of enlarged intra-PV membrane-bound structures containing host organelles**

Vps4A and Vps4B proteins are members of a class of hexameric AAA<sup>+</sup>-ATPases that disassemble protein complexes without degradation. Vps4 enzymes contain an N-terminal MIT domain that binds to the tails of ESCRT-III proteins. ESCRT-III/Vps4 complexes assemble within the necks of membrane tubules and convert the energy of ATP hydrolysis into pulling forces that sever the tubules (Yang et al., 2015). Vps4 is also required for the recycling of ESCRT-III from membrane-bound filaments back to the cytosol (Babst et al., 1998; Bishop and Woodman, 2000; Lin et al., 2005). As Vps4 is involved in many cellular processes that require membrane remodeling and scission, we hypothesize that *Toxoplasma* exploits host Vps4 along with CHMP4B to facilitate PVM budding and scission of IVN tubules, containing host organelles, from the PVM. We analyzed the distribution of Vps4A in infected cells transfected with mCherry-Vps4A. In transfected HeLa cells, we observed a perivacuolar staining for mCherry-Vps4A with puncta associated with the PV (Fig. 5 A). Expression of the DN mutant Vps4A<sup>EQ</sup> (with a mutation in the ATPase active site) causes a class E phenotype with an aggregation of MVB due to blockade of ESCRT-dependent ILV formation (Bishop and Woodman, 2000). We examined if Vps4A<sup>EQ</sup> mediated ESCRT-III dysfunction impacts PV sequestration of host organelles. In HeLa cells transfected with mCherry-Vps4A<sup>EQ</sup>, enlarged endosomal vacuoles were observed, with some surrounding the PV (Fig. 5A), as observed previously (Rivera-Cuevas et al., 2021). We noticed that in cells expressing mCherry-Vps4A<sup>EQ</sup> the PVM appeared less well-defined, as illustrated by an abnormal TgGRA7 staining almost filling the PV lumen, as opposed to a more circumferential TgGRA7 staining on PVM in cells expressing mCherry-Vps4AWT. Some host Rab11A vesicles could be identified by anti-Rab11A antibodies, that appeared to associate with the PV, however, due to the PVM abnormal morphology, we were unable to determine their localization outside versus inside the PV.

To investigate the morphological PVM defects and assess the PV for host organelle sequestration, we conducted TEM analyses on infected HeLa cells transfected with mCherry-Vps4<sup>EQ</sup>. Expectedly, in transfected cells incubated with LDL-gold particles, we detected gold particles in enlarged multilamellar organelles accumulated in the host cytoplasm (Fig. 5 B), with some clustering around the PV (Fig. 5 C). A striking observation was the presence of large PVM-derived membranous whorls that expand into the vacuolar space (Fig. 5 C and D); some IVN tubules were seen attached to these enlarged structures (Fig. 5 D, right inset). Intra-PV LDL-gold-containing organelles amassed in bundles forming large multi-vesiculated entities up to 900 nm in diameter (Fig. 5 D) versus the small intra-PV, LDL-gold-containing

organelles in the PV of non-transfected cells (~200 nm in diameter) (Fig. 1 B, panel c and Coppens et al., 2006). These LDL-gold-containing organelles remained close to the PVM (average distance of ~0.25  $\mu$ m), whereas in WT PV many were present in the PV center (Fig. 5 F). Altogether, these observations reveal that Vps4A DN causes abnormal PVM proliferation with host organelles entrapped in PVM folds, suggesting retardation of scission activities due to impaired Vps4A functions.

### **Intra-PV Rab11A is surrounded by host ALG-2, an interacting partner of the ESCRT accessory protein ALIX**

ALIX, an adaptor protein whose Bro1 domain binds to a C-terminal motif of CHMP4, participates in a variety of ESCRT-III-mediated membrane remodeling processes (McCullough et al., 2008). The calcium-binding protein ALG-2 forms intramolecular interactions with ALIX in a  $\text{Ca}^{2+}$ -dependent manner (Sun et al., 2015). Host ALIX and ALG-2 have been shown to associate with the *Toxoplasma* PV as puncta along and within the PV (Cygan et al., 2021; Rivera-Cuevas et al., 2021). To investigate if host ALIX or ALG-2 participate in host vesicle internalization into the PV, we examined the distribution of intra-PV ALIX or ALG-2 puncta relative to Rab11A vesicles. In infected GFP-Rab11A-expressing VERO cells transfected with HA-tagged ALIX, only a few intra-PV ALIX-HA puncta displayed a partial overlap with GFP-Rab11A (Fig. 6 A). In comparison, the association of ALG-2-HA with the PVM and IVN was more prominent and numerous ALG-2-HA puncta partially overlapped with GFP-Rab11A (Fig. 6 B). To assess the overlap of GFP-Rab11A and ALG2-HA in finer detail, we performed dual immunogold labeling on ALG-2-HA expressing cells. In the mammalian cytoplasm, gold particles were observed on membranes and vesicles associated with either Rab11A or ALG-2-HA, but none with both (Fig. 6 A, panel a). Within the PV, however, both Rab11A and ALG-2-HA were detected on the same vesicular structures with Rab11A (10-nm-gold particles) on the inside and ALG-2-HA (5-nm-gold particles) externally displayed (Fig. 6 A, panels b-d). This illustrates that intra-PV Rab11A vesicles are surrounded by a membrane that contains ALG-2 (presumably derived from the PVM/IVN), suggesting a potential role for ALG-2, and to a lesser extent ALIX, in cooperating with CHMP4B at sites of PVM remodeling for host organelle sequestration.

### **The ESCRT-interacting proteins TgGRA14 and TgGRA64, secreted to the PVM, function synergically in Rab11A vesicle PV internalization**

*T. gondii* secretes two dense granule proteins, TgGRA14 and TgGRA64, that physically interact with several ESCRT components, and localize to the PVM and IVN post-secretion (Rivera-Cuevas et al., 2021; Mayoral et al., 2022). We examined the contribution of TgGRA14 and TgGRA64 in ESCRT-mediated PVM functions. First, we compared the PV distribution of GFP-CHMP4B (low level of

expression) between a strain lacking both *gra14* and *gra64* ( $\Delta gra14\Delta gra64$ ), and WT and  $\Delta gra2\Delta gra6$  parasites. GFP-CHMP4B was detected along the PVM of each strain, but few intra-PV GFP-CHMP4B puncta were observed like for  $\Delta gra2\Delta gra6$  PV (Fig. 7 A). This suggests that CHMP4B may associate with the PV independently of TgGRA14 and/or TgGRA64 but that these proteins are most likely involved in CHMP4B-mediated PVM invaginations. Inspection of  $\Delta gra14\Delta gra64$  ultrastructure did not reveal obvious defects of the PVM or host organelle association (Fig. 7 B, panel a). The PV contains an IVN (Fig. 7 B, panel b; Fig. S5, panel a) but also abnormal fibrous structures appended to IVN tubules (Fig. S5, panels b and c). No organellar abnormalities were observed for  $\Delta gra14$  or  $\Delta gra14\Delta gra64$  parasites, except for the accumulation of starch-like amylopectin granules (Fig. 7 B, panels c and d). Accumulation of amylopectin granules, a marker of stress (Coppin et al., 2003), suggest that parasites lacking TgGRA14 and/or TgGRA64 probably undergo remodeling of their metabolism to cope with stress conditions, such as nutrient limitations.

Second, we investigated whether  $\Delta gra14\Delta gra64$  and  $\Delta gra14$  parasites remodel their PVM to create buds or invaginations in cells transfected with DN CHMP4B-mEm. While the PVM of WT parasites displayed numerous, long tubular extensions enclosing CHMP4B-mEM filaments on each parasite section viewed (Fig. 7 C, panel a), the PVM of both mutants exhibited sparse buds (Fig. 7 C, panels b-d). In rare sections of either mutant, longer tubular invaginations were observed, containing inner filaments along the tubule membrane and displaying irregular constrictions (Fig. 7 D, panels a-c) or sometimes short ramifications (Fig. S5 B). In 22% of  $\Delta gra14\Delta gra64$  sections, no PVM budding or bending induced by CHMP4B filaments was apparent, reflecting the rarity of PVM remodeling events in the double mutant (Fig. S5 C).

Third, we compared the ability of  $\Delta gra14$ ,  $\Delta gra64$ ,  $\Delta gra14\Delta gra64$  and  $\Delta gra2\Delta gra6$  parasites to scavenge host Rab11A vesicles, relative to WT parasites; the  $\Delta gra2\Delta gra6$  mutant was used as a control as it was previously shown to have a defect in host vesicle internalization (Romano et al., 2017). VERO expressing GFP-Rab11A were infected to assess the number, distance from the PV centroid and size of intra-PV GFP-Rab11A puncta. Compared to WT parasites, both  $\Delta gra14$  and  $\Delta gra64$  parasites showed a statistically significant (~25% decrease) in the number of intra-PV host GFP-Rab11A puncta (Fig. 7 E and Fig. S6 A). A more pronounced reduction in puncta number was observed for  $\Delta gra14\Delta gra64$ , corresponding to a ~45% decrease compared to WT parasites, though still not as dramatic as for  $\Delta gra2\Delta gra6$  parasites (~70% decrease). No differences were observed in the distance to the PV centroid nor the volume of intra-PV GFP-Rab11A puncta, except for  $\Delta gra2\Delta gra6$  (Fig. S6 B and C).

TgGRA14 has been shown to co-immunoprecipitate with CHMP4B along with other ESCRT components (Rivera-Cuevas et al., 2021). Lastly, we assessed the distribution of TgGRA14 relative to CHMP4B at the PV by infecting HeLa cells stably expressing CHMP4B for 6 h and 24 h (Fig. 8 A). Unlike TgGRA7 that localizes all around the PVM, TgGRA14 appears more concentrated at some areas of the PV. Interestingly, the signal for GFP-CHMP4B was observed at the sites of TgGRA14 accumulation in well-distinct puncta. At 24 h p.i., TgGRA14 and GFP-CHMP4B were also observed in the same regions, inside the PV. Such a co-distribution of TgGRA14 and GFP-CHMP4B at the PV is in accordance with the TgGRA14-CHMP4B interactions.

Collectively, our data indicate a connection between the poor ability of *Toxoplasma* lacking *gra14* and *gra64* to remodel the PVM and their reduced competency in sequestering intra-PV host vesicles. However, the retention of some activity reveals that other protein/s may be able to recruit host ESCRT at the PVM and function analogously for host vesicle uptake. Our results suggest a synergistic role for TgGRA14 and TgGRA64, which both function to recruit host ESCRT components, in host vesicle uptake. It also emphasizes the foremost contribution of IVN tubules in entrapping host organelles.

## Discussion

*Toxoplasma* is proficient in manipulating its host cell to gain access to vital nutrients, either from the cytosol (e.g., molecules, proteins) or organelles (e.g., lipids). One strategy developed by *Toxoplasma* for nutrient import is the formation of inward PVM buds, creating a pathway for host material into the PV. TEM examinations of the PVM illustrate various size and shapes (from vesicular to tubular) of PVM buds. We previously described two types of PVM invaginations that are depicted in our model in Fig. 10 A: one generated by host microtubules recruited at the PV and poking into the PVM (Coppens et al., 2006), and the other mediated by IVN tubules secreted by *Toxoplasma* in the PV and fusing with the PVM (Romano et al., 2017). We also identified smaller PVM buds morphologically distinct from these two tubular PVM invaginations. Host endocytic structures are often observed encroached in these different PVM invaginations before being engaged deeper into the PV lumen. ESCRT proteins remodel membranes by creating indentations and forming a bridge between membranes to enable fusion and fission. *Toxoplasma* expresses two proteins (TgGRA14 and TgGRA64) previously shown to interact with ESCRT machinery at the PVM and IVN (Rivera-Cuevas et al., 2021; Mayoral et al., 2022). In this study, we investigated how *Toxoplasma* exploits host ESCRT machinery, by focusing on CHMP4B, ALIX, ALG-2, and Vps4, for PVM budding and scission in relation to intra-PV sequestration of host endocytic organelles. On the parasite side, we examined the contribution of the two ESCRT interactors, TgGRA14 and TgGRA64. Based on our findings and published data, we propose a model (Fig. 10 B) summarizing the interplay between these host and parasite proteins for entrapping some host organelles into the PV.

ESCRT proteins govern membrane remodeling processes that require stabilizing membrane curvature, such as the formation of endosomal ILV in MVB (Vietri et al., 2020; Schöneberg et al., 2017; Pfitzner et al., 2021; Hurley, 2015). Similar to budding of the MVB limiting membrane, we propose that ESCRT components recruited to the PV generate PVM invaginations protruding into the PV lumen. At the PV, ESCRT-III proteins would oligomerize to form tight filamentous structures around the neck of the budding PVM and Vps4 ATP hydrolysis would provide the force necessary for pinching off of PVM buds away from the host cytosol. Thus, formation of ILV from the MVB membrane and intra-PV vesicles/tubules from the PVM may be viewed as topologically comparable. Under expression of the DN mutant Vps4A<sup>EQ</sup>, very large membrane-bound compartments packed with many host endo-lysosomes are observed inside the PV, with morphology distinct from structures typically found in PV of WT, indicating that the lack of functional Vps4 interferes with proper internalization. The same phenotype is observed when FLAG-CHMP4B is overexpressed, with these large structures still connected to the PVM, suggesting impaired scission activity. While the Vps4 binding domain is near the C-terminal end of CHMP4B, it remains possible that the acidic FLAG tag interferes with the CHMP4B ANCHR domain that contributes to membrane binding and may impede proper ESCRT-III association with membranes and Vps4 function.

Aspects of ESCRT-III recruitment, however, would differ from ILV biogenesis as it would involve parasite proteins. For example, a bioinformatics analysis identified TSG101- and ALIX-targeting motifs in TgGRA14 that are exposed to the host cytosol; the *Δgra14* mutant diminishes PVM recruitment of endogenously expressed GFP-TSG101 but has no effect on ALIX, suggesting the involvement of additional parasite protein/s (Rivera-Cuevas et al., 2021). The parasite TgGRA64 protein was shown by co-immunoprecipitation and proximity labeling to interact with several host ESCRT components (CHMP4B, TSG101, ALG-2, ALIX) (Mayoral et al., 2022). Our immunofluorescence assays show that the *Δgra14Δgra64* mutant still recruits CHMP4B at the PVM, indicating the expression of other ESCRT recruiter/s that compensate for the loss of *gra14* and *gra64*. Indeed, immunoprecipitation and proximity-labeling assays of TgGRA14 or TgGRA64 have identified about 15 parasite proteins as potential candidates (Rivera-Cuevas et al., 2021) (Mayoral et al., 2022).

In *Toxoplasma*-infected epithelial cells, GFP-CHMP4B localizes to the host cytosol and nucleus with partial association of vesicles with the PVM and IVN; puncta on the IVN suggest that CHMP4B-containing buds formed at the PVM, are subsequently internalized into the PV at sites near the IVN. A recent publication on *Toxoplasma*-infected dendritic cells also reveals host CHMP4B at the PV though in this cell line CHMP4B relocalized almost completely to the PV, suggesting possible cell type variations (Croce et al., 2022). Overexpression of CHMP4B fused C-terminally with mEmerald generate impressive tubular PVM invaginations, enclosing CHMP4B spiral filaments. Membrane-associated ESCRT-III

usually has a short lifespan (Baumgärtel et al., 2011; Jouvenet et al., 2011) due to Vps4 activity in disassembling and recycling ESCRT-III subunits (Babst et al., 1998; Lin et al., 2005). Depletion of Vps4 can increase the lifetime of membrane-associated ESCRT-III, leading to the accumulation of plasma membrane ESCRT-III filaments, composed of uniform spiral assemblies with a mean outer diameter of 110 nm (Cashikar et al., 2014). Our DN CHMP4B-mEm system mimics Vps4 depletion, with the accumulation of stable PVM invaginations containing very long (up to 7  $\mu$ m) and narrow (110 nm in diameter) CHMP4B filaments, reflecting a blockage of PVM scission. The stabilization of CHMP4B in its assembled state within PVM invaginations may be due to poor access of Vps4 to the MIM domain of CHMP4B-mEm or insufficient amounts of Vsp4 enzyme to depolymerize all the CHMP4B filaments at the PVM. The parasite proteins TgGRA14 and TgGRA64 may induce PVM invaginations through interaction with ESCRT components (e.g., CHMP4, TSG101, ALIX) as fewer CHMP4B-mEm invaginations are detected, by EM, in the  $\Delta gra14$  mutant, with even fewer present in  $\Delta gra14\Delta gra64$ . Uniquely compared to other systems, CHMP4B-associated PVM buds/tubules seem to fuse with IVN tubules based on data showing sparse and short PVM invaginations in the  $\Delta gra2\Delta gra6$  mutant under DN CHMP4B-mEm conditions. Through this fusion, additional membranes may be supplied, creating deeper invaginations in which host material may remained trapped, with no possible return to the host cell.

In summary, this study has highlighted unique features of ESCRT-mediated processes at the *Toxoplasma* PV. First, intravacuolar membranous tubules likely attach to ESCRT-mediated buds to elongate the invaginations at the PVM prior to scission. Second, ESCRT-mediated invaginations can be involved in the internalization of cargos as large as endosomes or Rab vesicles into the PV. Thus, the ESCRT machinery appears to function in a process more akin to phagocytosis for the engulfment of large particles. Lastly, many parasite proteins and perhaps distinct complexes may be involved in interfacing with host ESCRT at the PV. To this point, the  $\Delta gra14\Delta gra64$  mutant has a greater defect in host Rab11A vesicle internalization and in the formation of CHMP4B-mEmerald induced PVM invaginations than single mutants, suggesting a synergistic role for TgGRA14 and TgGRA64 at the PVM/IVN through interactions with specific ESCRT components.

## Materials and Methods

### Reagents and antibodies

All reagents were obtained from Sigma-Aldrich, unless otherwise stated. The following primary antibodies were used in this study: rat monoclonal and rabbit polyclonal anti-GRA7 (Coppens et al., 2006) and rabbit anti-GRA14 (graciously provided by Dr. Yoshifumi Nishikawa, Obihiro University of Agriculture and Veterinary Medicine, Obihiro, Japan; Ihara et al., 2020). Commercial antibodies include rabbit polyclonal anti-Rab11A (Cell Signaling, Danvers, MA, 2413S), rabbit polyclonal anti-GFP



antibodies (Thermo Fisher Scientific, A6455), mouse monoclonal anti-HA.11 (clone 16B12; Biolegend, San Diego, CA, 901516), and mouse monoclonal anti-FLAG (clone M2; Sigma, F1804). Secondary antibodies used were: goat anti-rat, anti-rabbit and anti-mouse conjugated to Alexa Fluor 488, 594, or 350 (Thermo Fisher Scientific).

### Mammalian cell and parasite culture

Human foreskin fibroblasts (HFF), HeLa and VERO cells were obtained from the American Type Culture Collection (Manassas, VA). VERO stably expressing GFP-Rab11A was described previously (Romano et al., 2017). HeLa cells stably expressing GFP-CHMP4B were generously provided by Dr. Phyllis Hanson (University of Michigan, Ann Arbor, MI; Jouvenet et al., 2011) and authenticated by siRNA of CHMP4B (Fig. S1A). All cells were grown in alpha-minimum essential medium (Alpha MEM) supplemented with 10% fetal bovine serum (FBS), 2 mM glutamine and penicillin/streptomycin (100 units/ml per 100 µg/ml) and maintained at 37°C in 5% CO<sub>2</sub> and checked for any contamination. The tachyzoite RH strain (type I lineage) of *Toxoplasma* was used in this study. RH deleted for both *gra2* and *gra6* ( $\Delta gra2\Delta gra6$ ) was generously provided by Dr. M.-F. Cesbron-Delauw (Université Grenoble Alpes, Grenoble, France; (Mercier et al., 2002)). Generation of the RH  $\Delta gra14$  strain was described previously (Rivera-Cuevas et al., 2021). The RH  $\Delta gra64$  strain (made in a  $\Delta ku80\Delta hxgprt$  background for easier genetic manipulation) was generated identically to the  $\Delta gra64$  strains described in (Mayoral et al., 2022). The  $\Delta gra14\Delta gra64$  strain was generated from the RH  $\Delta gra64$  strain as follows: first, CRISPR-Cas9 gene editing was used to target the endogenous *GRA14* locus by transfecting 7.5 µg of a vector expressing an HXGPRT resistance cassette and Cas9 with the guide RNA sequence 5' – CCAGAGACCAAGCGAATAGA – 3', along with 1.5µg of a repair template generated by PCR (Forward primer: 5'– TCCGAGTTTACACAGGCTGGGCTACCAGAGACCAAGCGAAGAACAGAACTGATCTCAGA– 3'; Reverse primer: 5'– GGTTCCCGATTGGTCTACATTACTGACTTCAACCCTTCTAAAGATCCTCTTCGGAAATAA – 3'), designed to insert three copies of the myc epitope-tag at the C-terminus of the gene for the purposes of confirming the absence of endogenous GRA14 protein after gene knockout. Following transfection, parasites were selected for in mycophenolic acid (25 µg/mL) and xanthine (50 µg/mL) for one week. Transfected parasites were subcloned by limiting dilution in 96-well plates. Successful tagging was demonstrated by IFA using anti-myc tag antibody and by Sanger Sequencing the PCR products amplified from genomic DNA, using the following primers to amplify the C-terminus of GRA14: 5'– CGCCGAACCTGAACACAGAT – 3' and 5' – ATCACGCGTTCAATCACATC – 3'. After generating a  $\Delta gra64, GRA14\text{-}3xMyc$  parasite strain, a CRISPR-Cas9 strategy was again used as described above, transfecting parasites with 7.5 µg of a Cas9 vector containing the guide RNA sequence 5'–

GCGCGGGGGGACCGCTCGTC - 3' (targeting the *GRA14* start codon region) along with 280 pmol unannealed 100bp donor oligos containing homologous arms and multiple stop codons in place of the endogenous GRA14 start codon (5' – CCACTGCTAAGCACAAAATGCAGGCGATAGCGCGGGGGGTAAGTACTGACTGACTAGCTAACGG GACCGCTCGTCGGGGTGGTCGAGTTGTAGCTGGCTTTTC -3', and the reverse complement of this sequence). Selection, subcloning, and knockout screening was performed as described above, using the following primers to amplify the 5'UTR and N-terminus region of the GRA14 locus to confirm the insertion of stop codons as designed: 5'- AGAAAGCGTCACTCAGACAT – 3' and 5' – CTCCTAGATAGCTTACGGGC – 3'. All parasites were propagated by serial passage in monolayers of HFF (Roos et al., 1994; Khan and Grigg, 2017).

### Plasmids

Plasmids used in this study include mEmerald-Mito-7 (a gift from Dr. Michael Davidson (Addgene plasmid # 54160 ; <http://n2t.net/addgene:54160> ; RRID:Addgene\_54160)), mEmerald-MAP4-C-10 (a gift from Dr. Michael Davidson (Addgene plasmid # 54152 ; <http://n2t.net/addgene:54152> ; RRID:Addgene\_54152)), (Planchon et al., 2011). ALIX-HA and ALG-2-HA (generously provided by Dr. John Boothroyd, Stanford University, Stanford, CA, (Cygan et al., 2021). FLAG-CHMP4B (kindly provided by Dr. Phyllis Hanson, University of Michigan, Ann Arbor, MI), mCherry-N1-VPS4A and mCherry-N1-VPS4A EQ (graciously provided by Dr. Akira Ono, University of Michigan, Ann Arbor, MI (Rivera-Cuevas et al., 2021)) and pCHMP4B-mCherry (generously provided by Dr. Jennifer Lippincott-Schwartz, Janelia Research Campus, Ashburn VA (Elia et al., 2011)).

To generate a plasmid with CHMP4B tagged at the 3'end with mEmerald, we amplified CHMP4B from pCHMP4B-mCherry using primers CHMP4B\_Cterm forward (5' ATCCGCTAGCATGTCGGTGTTCGGGAAG 3') and CHMP4B\_C-term reverse (5' GTGGATCCCCCATGGATCCAGCCCAGTTC 3') and we amplified mEmerald including vector sequence but omitting the mitochondrial targeting sequence from the mEmerald-Mito-7 plasmid using primers mEmeraldVector forward (5' TGGATCCATGGGGGATCCACCGGTCGCC 3') and mEmeraldVector reverse (5' ACACCGACATGCTAGCGGATCTGACGGTTCAC 3') and combined the fragments using a HiFi assembly kit (New England Biolabs, Ipswich, MA) to create a plasmid expressing CHMP4B-mEmerald, with a 7aa linker between CHMP4B and mEmerald. To generate a plasmid with CHMP4B tagged at the 5' end with mEmerald, we amplified CHMP4B from pCHMP4B-mCherry using primers NlinkCHMP4B\_fwd (5' GCTGTACAAGTCCGGACTCAGATCT 3') and NlinkCHMP4B\_rev (5' CGGTGGATCCTTACATGGATCCAGCCCAG 3'), mEmerald from mEmerald-MAP4-C-10 using primers N\_Emerald\_fwd (5' GGTCGCCACCATGGTGAGCAAGGGCGAG 3') and N\_Emerald\_rev (5'

TGAGTCCG GACTTGTACAGCTCGTCCATGC 3'), and vector sequence from mEmerald-MAP4-C-10 using mEmMAPVector\_fwd (5' ATCCATGTAAAGGATCCACCGGATCTAGATAACTGATCATAATCAGC 3') and mEmMAPVector\_rev (5' TGCTCACCATGGTGGCGACCGGTAGCGC 3') and combined the fragments using a HiFi assembly kit to create a plasmid expressing mEmerald-CHMP4B, with a 12aa linker between mEmerald and CHMP4B.

### **LDL-gold preparation**

Human LDL was isolated from fresh serum by zonal density gradient ultracentrifugation as described (Poumay and Ronveaux-Dupal, 1985). Briefly, the density of human serum was increased to 1.25 g/ml with KBr, centrifuged at 81,900 g x min (Beckman MLA-80 rotor; Beckman Instruments, Inc., Palo Alto, CA) for 24 h at 4°C. The supernatant (lipoproteins) was collected, adjusted to the density of 0.126 g/ml, placed in the bottom of a centrifuge tube, and layered on top with 0.9% NaCl (1:5 vol/vol). After ultracentrifugation at 81,900 g x min for 6 h at 4°C, LDL (middle, yellow layer) was collected, extensively dialyzed against 2 mM sodium borate pH 9, and filtered with a 0.2 µm PVDF syringe filter and stored at 4°C. For the coupling reaction of LDL to gold particles of 15 nm in diameter, a solution of 0.3 mM tetrachloroauric acid was reduced with 1.16mM sodium citrate as described (De Roe et al., 1987) except for the addition of 0.00015% tannic acid for gold stabilization under boiling until the mixture became dark red. For LDL-gold complex preparation, a solution of LDL adjusted at 0.2 mg/ml was added to a solution of gold particles at 57 µg/ml (1:5, vol/vol) for 30 min with gently agitation before addition of 1 ml of 1% BSA in 2 mM sodium borate pH 9. After 5 min, 5 ml of LDL-gold conjugate were layered on 1 ml of a 1.15 M sucrose cushion and sedimented at 97,500 g x min using a Beckman T150 rotor. The solution of LDL-gold conjugates collected from the sucrose solution were dialyzed against PBS before use.

### **Transfection and parasite infection**

For fluorescence microscopy, HeLa cells were transiently transfected according to the manufacturer's instructions for JetPrime (Polyplus, Illkirch, France). HeLa cells (50,000) were seeded to coverslips the day before transfection. For the transfection, 0.2 µg DNA in 50 µl JetPrime buffer was mixed with 0.4 µl JetPrime reagent and incubated at room temperature for 10 min prior to addition to cells. VERO cells expressing GFP-Rab11A (40,000) were seeded to coverslips the day before transfection. For the transfection, 0.8 µg of DNA in 50 µl JetOptimus buffer (Polyplus) was mixed with 0.75 µl JetOptimus reagent and incubated at room temperature for 10 min prior to addition to the cells. For EM, HeLa cells were grown in 6-well plates to 60% confluency and transiently transfected with plasmid DNA (1 µg per

well) mixed with JetOptimus reagent (1  $\mu$ l per well) and incubated at room temperature for 10 min, according to manufacturer's instructions (Polyplus) before adding to cells. All transfected cells were incubated at 37°C with 5% CO<sub>2</sub> for 4 h, washed with PBS and allowed to recover for 1 h at 37°C with 5% CO<sub>2</sub> prior to infection with parasites. For infection, freshly egressed parasites were added to the cells for 1 h, washed with PBS to remove extracellular parasites and incubated for times indicated in Alpha MEM. For some samples, LDL complexed with gold was added in Alpha MEM medium with 10% (vol/vol) of delipidated FBS (Cocalico Biologicals, Stevens, PA) and the cells were incubated at 37°C in 5% CO<sub>2</sub> for 20 h. Infected cells were fixed for either fluorescence microscopy or EM.

### **siRNA**

HeLa cells stably expressing GFP-CHMP4B were seeded to coverslips and grown to 50% confluency. The cells were transfected using JetPrime according to manufacturer's instructions. The cells were transfected with siRNA control (ON-TARGET plus Non-targeting pool, 5 nmol; D-001810-10-05; Dharmacon/Horizon Discovery, Waterbeach, GB) or CHMP4B siRNA (ON-TARGET plus Human CHMP4B (128866) – SMART pool, 5 nmol; L-018075-01-0005; Dharmacon/Horizon Discovery) using 27.5 pmoles of siRNA. Samples were fixed at 24, 48, and 72 h post-transfection and mounted with ProLong Glass mounting medium.

### **Cell Labeling**

For immunolabeling, cells were fixed in PBS with 4% formaldehyde (Polysciences, Inc.) and 0.02% glutaraldehyde for 15 min. Cells were permeabilized with 0.3% Triton X-100 in PBS for 5 min and washed twice with PBS before blocking. Cells were incubated in blocking buffer (3% BSA, Fraction V; Thermo Fisher Scientific) in PBS for 1 h followed by incubation in primary antibodies diluted in blocking buffer (1:800 for anti-GRA7; 1:1000 for anti-HA; 1:1500 for anti-FLAG; 1:100 for anti-Rab11A; 1:500 for anti-GRA14 for 1 h to overnight (anti-Rab11A only). Cells were washed three times with PBS for 5 min each and then incubated in secondary antibody diluted (1:2000) in blocking buffer for 45 min to 1 h followed by three washes with PBS for 5 min each. In some cases, cells were incubated in a 1:1000 dilution of 1 mg/ml DAPI (Roche Diagnostics) in PBS for 5 min followed by three washes with PBS. Coverslips were rinsed with water and mounted on slides with ProLong Diamond mounting solution.

### **Fluorescence microscopy**

Fixed samples were viewed with a Zeiss AxioImager M2 fluorescence microscope equipped with an oil-immersion Zeiss plan Apo 100x/NA1.4 objective or a Zeiss EC plan Neo 40x/NA0.75 objective (siRNA samples) and a Hamamatsu ORCA-R2 camera. Optical z-sections with 0.2  $\mu$ m spacing were acquired

using Volocity software (Quorum Technologies, Puslinch, ON, Canada). For siRNA samples, only a single z-plane was acquired.

### Image analysis

Images were deconvolved with an iterative restoration algorithm using calculated point spread functions and a confidence limit of 100% and iteration limit of 30-35 using Volocity software. Images were cropped and adjusted for brightness and contrast using Volocity software. Figures were compiled in Adobe Illustrator.

To characterize the intra-PV GFP-Rab11A foci, we acquired optical z-sections of infected cells with PV containing 8 parasites, to normalize for PV size. After deconvolution, images were analyzed with a measurement protocol generated in Volocity (Quorum Technologies) according to published protocols with some modifications (Romano et al., 2017, 2021). The measurement protocol measured objects in 3D reconstructed volumes of optical z-slices. The PV was identified by the fluorescence intensity of TgGRA7 signal; thresholds were set manually by using the outer TgGRA7 PVM staining as the boundary of the PV and the minimum object size was set to  $20 \mu\text{m}^3$ . To close any holes in the identified structure, the close function was used with 20 iterations. GFP-Rab11A puncta were identified by fluorescence intensity (automatic thresholds with an offset threshold ranging from 110 – 170%, minimum object size of  $0.4 \mu\text{m}^3$ ), noise was removed using a medium filter, and objects were separated using the “separate touching objects” tool with an object size guide of  $0.1 \mu\text{m}^3$ . Lastly, the compartmentalize function was used to identify GFP-Rab11A objects inside the PV. The number and volume of GFP-Rab11A puncta inside the PV were calculated plus the distance of the intra-PV GFP-Rab11A puncta to the PV centroid. To assess the number of GFP-CHMP4B puncta associated with the PV, optical z-sections of infected cells were acquired, deconvolved, and measured using the following measurement protocols in Volocity: the PV was identified with the ‘Find Objects Measurement’ tool using TgGRA7 fluorescence with automatic thresholding and a minimum object size of  $10 \mu\text{m}^3$ . Next, GFP-CHMP4B was identified with the ‘Find Objects Measurement’ tool based on GFP fluorescence with thresholding using standard deviation intensity (lower limit of 1) and a minimum object size of  $0.1 \mu\text{m}^3$ . Lastly, the ‘Compartmentalize’ tool was used to determine the number of GFP-CHMP4B puncta inside the PV.

Mander’s colocalization coefficients (MCC) were calculated using Volocity software (Quorum Technologies) along with a product of the difference of the means map (PDM), which is generated by identifying voxels where each signal is above its mean value after thresholding for background. Thresholds were set by measuring, using an ROI, the fluorescence intensity of each channel in a region of the nucleus without staining for either signal (background) (Fig. S2). In all other instances, thresholds were set by measuring, using an ROI, the fluorescence intensity of each channel in a region between cells.

These background values (per image) were used to calculate MCC and PDM values of the corresponding individual infected cells. The positive PDM shows voxels where both fluorescence signals are above the mean and show positive correlation.

For each siRNA sample, 15 random fields were captured as a single z-plane. To measure fluorescence intensity, an ROI encompassing the entire field was drawn and the mean fluorescence intensity was measured using Velocity software. Intensity values were plotted using GraphPad Prism.

### **Transmission Electron Microscopy (TEM)**

For thin-section TEM, cells were fixed in 2.5% glutaraldehyde (Electron Microscopy Sciences; EMS, Hatfield, PA) in 0.1 M sodium cacodylate buffer (pH 7.4) for 1 h at room temperature, and processed as described (Fölsch et al., 2001).

For immunogold staining, cells were fixed in 4% paraformaldehyde (Electron Microscopy Sciences) in 0.25 M HEPES (pH7.4) for 1 h at room temperature, and then in 8% paraformaldehyde in the same buffer overnight at 4°C. They were infiltrated, frozen and sectioned as described (Romano et al., 2017). The sections were immunolabeled with antibodies against GFP at 1:10, HA at 1:50 or Rab11A at 1:10 diluted in PBS/1% fish skin gelatin, and then with secondary IgG antibodies coupled to 10 nm protein A-gold particles before examination with a Philips CM120 EM or a Hitachi 7600 EM under 80 kV, equipped with a dual AMT CCD camera system. The AMT v6.1 software was used for quantitative measurement of the diameter of PVM invaginations with CHMP4B-mEm (from 62 invaginations from 26 different PV sections) and of intra-PV host organelle size and distance performed on 19 to 23 representative PV sections.

### **Statistical analysis**

Numerical data are presented as means  $\pm$  SD or in dot plots with means indicated (GraphPad Prism, San Diego, CA). To compare samples, we used a one-way ANOVA with a Tukey's multiple comparisons test or unpaired two-tailed t-tests using GraphPad Prism.

### **Acknowledgements**

We thank the members of the Coppens' laboratory for helpful discussion during the course of this work and especially Karen Ehrenman for her help in cloning the mEmerald-CHMP4B and CHMP4B-mEmerald plasmids. We are grateful to Phyllis Hanson for helpful advice and discussions related to this work. We also thank the generous providers of plasmids and parasite strains used in this study. We thank the excellent technical staff from Electron Microscopy Core facilities at Johns Hopkins University School



of Medicine (M. Delannoy, B. Smith) and Yale University School of Medicine (K. Zichichi). This study was supported by a grant from the NIH R01 AI060767 to I.C and NIH R01 AI134753 to LMW.

The authors declare no competing financial interests.

### Author Contributions

Conceptualization: JDR, IC, JM, LMW, VBC

Data curation: JDR, IC

Formal analysis: JDR, IC

Funding acquisition: IC

Investigation: IC, JDR

Methodology: JDR, IC, JM, RBG

Resources: JDR, IC, JM, RBG, YR

Validation: JDR, IC

Visualization: JDR, IC

Writing – original draft: JDR, IC

Writing – review & editing: JDR, IC, JM, RBG, YR, LMW, VBC

### References

- Alonso Y Adell, M., S.M. Migliano, and D. Teis. 2016. ESCRT-III and Vps4: a dynamic multipurpose tool for membrane budding and scission. *The FEBS Journal*. 283:3288–3302. doi:10.1111/febs.13688.
- Babst, M., B. Wendland, E.J. Estepa, and S.D. Emr. 1998. The Vps4p AAA ATPase regulates membrane association of a Vps protein complex required for normal endosome function. *EMBO J*. 17:2982–2993. doi:10.1093/emboj/17.11.2982.
- Baumgärtel, V., S. Ivanchenko, A. Dupont, M. Sergeev, P.W. Wiseman, H.-G. Kräusslich, C. Bräuchle, B. Müller, and D.C. Lamb. 2011. Live-cell visualization of dynamics of HIV budding site interactions with an ESCRT component. *Nat Cell Biol*. 13:469–474. doi:10.1038/ncb2215.
- Bishop, N., and P. Woodman. 2000. ATPase-defective Mammalian VPS4 Localizes to Aberrant Endosomes and Impairs Cholesterol Trafficking. *Mol Biol Cell*. 11:227–239.
- Bittame, A., G. Effantin, G. Pètre, P. Ruffiot, L. Travier, G. Schoehn, W. Weissenhorn, M.-F. Cesbron-Delauw, J. Gagnon, and C. Mercier. 2015. *Toxoplasma gondii*: Biochemical and biophysical characterization of recombinant soluble dense granule proteins GRA2 and GRA6. *Biochem Biophys Res Commun*. 459:107–112. doi:10.1016/j.bbrc.2015.02.078.

- Cashikar, A.G., S. Shim, R. Roth, M.R. Maldazys, J.E. Heuser, and P.I. Hanson. 2014. Structure of cellular ESCRT-III spirals and their relationship to HIV budding. *eLife*. 3:e02184. doi:10.7554/eLife.02184.
- Coppens, I., J.D. Dunn, J.D. Romano, M. Pypaert, H. Zhang, J.C. Boothroyd, and K.A. Joiner. 2006. *Toxoplasma gondii* Sequesters Lysosomes from Mammalian Hosts in the Vacuolar Space. *Cell*. 125:261–274. doi:10.1016/j.cell.2006.01.056.
- Coppin, A., F. Dzierszinski, S. Legrand, M. Mortuaire, D. Ferguson, and S. Tomavo. 2003. Developmentally regulated biosynthesis of carbohydrate and storage polysaccharide during differentiation and tissue cyst formation in *Toxoplasma gondii*. *Biochimie*. 85:353–361. doi:10.1016/S0300-9084(03)00076-2.
- Croce, C., F. Garrido, S. Dinamarca, J. Santi-Rocca, S. Marion, N. Blanchard, L.S. Mayorga, I. Cesbrian. 2022. Efficient cholesterol transport in dendritic cells defines optimal exogenous antigen presentation and *Toxoplasma gondii* proliferation. *Front Cell Dev Biol*. 10:837574. doi: 10.3389/fcell.2022.837574.
- Cygan, A.M., P.M.J. Beltran, A.G. Mendoza, T.C. Branon, A.Y. Ting, S.A. Carr, and J.C. Boothroyd. 2021. Proximity-Labeling Reveals Novel Host and Parasite Proteins at the *Toxoplasma* Parasitophorous Vacuole Membrane. *mBio*. doi:10.1128/mBio.00260-21.
- De Roe, C., P.J. Courtoy, and P. Baudhuin. 1987. A model of protein-colloidal gold interactions. *J Histochem Cytochem*. 35:1191–1198. doi:10.1177/35.11.3655323.
- Dou, Z., O.L. McGovern, M. Di Cristina, and V.B. Carruthers. 2014. *Toxoplasma gondii* Ingests and Digests Host Cytosolic Proteins. *mBio*. 5:e01188-14. doi:10.1128/mBio.01188-14.
- Elia, N., R. Sougrat, T.A. Spurlin, J.H. Hurley, and J. Lippincott-Schwartz. 2011. Dynamics of endosomal sorting complex required for transport (ESCRT) machinery during cytokinesis and its role in abscission. *Proc Natl Acad Sci USA*. 108:4846–4851. doi:10.1073/pnas.1102714108.
- Fölsch, H., M. Pypaert, P. Schu, and I. Mellman. 2001. Distribution and Function of Ap-1 Clathrin Adaptor Complexes in Polarized Epithelial Cells. *J Cell Biol*. 152:595–606.
- Griffith, M.B., C.S. Pearce, A.T. Heaslip. 2022. Dense granule biogenesis, secretion, and function in *Toxoplasma gondii*. *J. Eukaryot Microbiol*. 69:e12904. doi: 10.1111/jeu.12904.
- Guérin, A., R.M. Corrales, M.L. Parker, M.H. Lamarque, D. Jacot, H. El Hajj, D. Soldati-Favre, M.J. Boulanger, and M. Lebrun. 2017. Efficient invasion by *Toxoplasma* depends on the subversion of host protein networks. *Nat Microbiol*. 2:1358–1366. doi:10.1038/s41564-017-0018-1.
- Harker-Kirschneck, L., B. Baum, and A. Šarić. 2019. Changes in ESCRT-III filament geometry drive membrane remodelling and fission in silico. *BMC Biology*. 17:82. doi:10.1186/s12915-019-0700-2.
- Hartman, E.J., B. Asady, J.D. Romano, and I. Coppens. 2022. The Rab11-Family Interacting Proteins reveal selective interaction of mammalian recycling endosomes with the *Toxoplasma* parasitophorous vacuole in a Rab11- and Arf6-dependent manner. *Mol Biol Cell*. mbc.E21-06-0284. doi:10.1091/mbc.E21-06-0284.

- Henne, W.M., N.J. Buchkovich, Y. Zhao, and S.D. Emr. 2012. The endosomal sorting complex ESCRT-II mediates the assembly and architecture of ESCRT-III helices. *Cell*. 151:356–371. doi:10.1016/j.cell.2012.08.039.
- Howard, T.L., D.R. Stauffer, C.R. Degenin, and S.M. Hollenberg. 2001. CHMP1 functions as a member of a newly defined family of vesicle trafficking proteins. *J Cell Sci*. 114:2395–2404. doi:10.1242/jcs.114.13.2395.
- Ihara, F., R.M. Fereig, Y. Himori, K. Kameyama, K. Umeda, S. Tanaka, R. Ikeda, M. Yamamoto, Y. Nishikawa. 2020. *Toxoplasma gondii* dense granule proteins 7, 14, and 15 are involved in modification and control of the immune response mediated via NF- $\kappa$ B Pathway. *Front Immunol*. 11:1709. doi: 10.3389/fimmu.2020.01709.
- Hurley, J.H. 2015. ESCRTs are everywhere. *The EMBO J*. 34:2398–2407. doi:10.15252/emboj.201592484.
- Jouvenet, N., M. Zhadina, P.D. Bieniasz, and S.M. Simon. 2011. Dynamics of ESCRT protein recruitment during retroviral assembly. *Nat Cell Biol*. 13:394–401. doi:10.1038/ncb2207.
- Katoh, K., H. Shibata, H. Suzuki, A. Nara, K. Ishidoh, E. Kominami, T. Yoshimori, and M. Maki. 2003. The ALG-2-interacting Protein Alix Associates with CHMP4b, a Human Homologue of Yeast Snf7 That Is Involved in Multivesicular Body Sorting. *J Biol Chem*. 278:39104–39113. doi:10.1074/jbc.M301604200.
- Khan, A., and M.E. Grigg. 2017. *Toxoplasma gondii*: Laboratory Maintenance and Growth. *Curr Protoc Microbiol*. 44:20C.1.1–20C.1.17. doi:10.1002/cpmc.26.
- Lata, S., M. Roessle, J. Solomons, M. Jamin, H.G. Göttlinger, D.I. Svergun, and W. Weissenhorn. 2008. Structural basis for auto-inhibition of ESCRT-III CHMP3. *J Mol Biol*. 378:818–827. doi:10.1016/j.jmb.2008.03.030.
- Lin, Y., L.A. Kimpler, T.V. Naismith, J.M. Lauer, and P.I. Hanson. 2005. Interaction of the Mammalian Endosomal Sorting Complex Required for Transport (ESCRT) III Protein hSnf7-1 with Itself, Membranes, and the AAA+ ATPase SKD1. *J Biol Chem*. 280:12799–12809. doi:10.1074/jbc.M413968200.
- Magno, R.C., L. Lemgruber, R.C. Vommoro, W. De Souza, and M. Attias. 2005. Intravacuolar network may act as a mechanical support for *Toxoplasma gondii* inside the parasitophorous vacuole. *Microsc Res Tech*. 67:45–52. doi:10.1002/jemt.20182.
- Martin-Serrano, J., A. Yaravoy, D. Perez-Caballero, and P.D. Bieniasz. 2003. Divergent retroviral late-budding domains recruit vacuolar protein sorting factors by using alternative adaptor proteins. *Proc Natl Acad Sci USA*. 100:12414–12419. doi:10.1073/pnas.2133846100.
- Maxfield, F.R., and T.E. McGraw. 2004. Endocytic recycling. *Nat Rev Mol Cell Biol*. 5:121–132. doi:10.1038/nrm1315.

- Mayoral, J., R.B. Guevara, Y. Rivera-Cuevas, V. Tu, T. Tomita, J.D. Romano, L. Gunther-Cummins, S. Sidoli, I. Coppens, V.B. Carruthers, and L.M. Weiss. 2022. Dense granule protein, GRA64 interacts with host cell ESCRT proteins during *Toxoplasma gondii* infection. *mBio*. 13:e0144222. doi: 10.1128/mbio.01442-22.
- McCullough, J., A.K. Clippinger, N. Talledge, M.L. Skowrya, M.G. Saunders, T.V. Naismith, L.A. Colf, P. Afonine, C. Arthur, W.I. Sundquist, P.I. Hanson, and A. Frost. 2015. Structure and membrane remodeling activity of ESCRT-III helical polymers. *Science*. 350:1548–1551. doi:10.1126/science.aad8305.
- McCullough, J., R.D. Fisher, F.G. Whitby, W.I. Sundquist, and C.P. Hill. 2008. ALIX-CHMP4 interactions in the human ESCRT pathway. *Proc Natl Acad Sci U S A*. 105:7687–7691. doi:10.1073/pnas.0801567105.
- Melo, E.J.T. de, T.U. de carvalho, and W. de Souza. 1992. Penetration of *Toxoplasma gondii* into Host Cells Induces Changes in the Distribution of the Mitochondria and the Endoplasmic Reticulum. *Cell Structure and Function*. 17:311–317. doi:10.1247/csf.17.311.
- Melo, E.J.T., and W. de Souza. 1997. Relationship between the Host Cell Endoplasmic Reticulum and the Parasitophorous Vacuole Containing *Toxoplasma gondii*. *Cell Struct Func*. 22:317–323. doi:10.1247/csf.22.317.
- Mercier, C., and M.-F. Cesbron-Delauw. 2015. *Toxoplasma* secretory granules: one population or more? *Trends Parasitol*. 31:60–71. doi:10.1016/j.pt.2014.12.002.
- Mercier, C., J.-F. Dubremetz, B. Rauscher, L. Lecordier, L.D. Sibley, and M.-F. Cesbron-Delauw. 2002. Biogenesis of Nanotubular Network in *Toxoplasma* Parasitophorous Vacuole Induced by Parasite Proteins. *Mol Biol Cell*. 13:2397–2409. doi:10.1091/mbc.e02-01-0021.
- Muzioł, T., E. Pineda-Molina, R.B. Ravelli, A. Zamborlini, Y. Usami, H. Göttlinger, and W. Weissenhorn. 2006. Structural basis for budding by the ESCRT-III factor CHMP3. *Dev Cell*. 10:821–830. doi:10.1016/j.devcel.2006.03.013.
- Obita, T., S. Saksena, S. Ghazi-Tabatabai, D.J. Gill, O. Perisic, S.D. Emr, and R.L. Williams. 2007. Structural basis for selective recognition of ESCRT-III by the AAA ATPase Vps4. *Nature*. 449:735–739. doi:10.1038/nature06171.
- Panas, M.W., and J.C. Boothroyd. 2021. Seizing control: how dense granule effector proteins enable *Toxoplasma* to take charge. *Mol Microbiol*. 115:466–477. doi:10.1111/mmi.14679.
- Pernas, L., Y. Adomako-Ankomah, A.J. Shastri, S.E. Ewald, M. Treeck, J.P. Boyle, and J.C. Boothroyd. 2014. *Toxoplasma* Effector MAF1 Mediates Recruitment of Host Mitochondria and Impacts the Host Response. *PLOS Biology*. 12:e1001845. doi:10.1371/journal.pbio.1001845.
- Pernas, L., and J.C. Boothroyd. 2010. Association of host mitochondria with the parasitophorous vacuole during *Toxoplasma* infection is not dependent on rhopty proteins ROP2/8. *Int J Parasitol*. 40:1367–1371. doi:10.1016/j.ijpara.2010.07.002.

- Pfützner, A.-K., J. Moser von Filseck, and A. Roux. 2021. Principles of membrane remodeling by dynamic ESCRT-III polymers. *Trends in Cell Biol.* 31:856–868. doi:10.1016/j.tcb.2021.04.005.
- Piper, R.C., and D.J. Katzmann. 2007. Biogenesis and Function of Multivesicular Bodies. *Annu Rev Cell Dev Biol.* 23:519–547. doi:10.1146/annurev.cellbio.23.090506.123319.
- Planchon, T.A., L. Gao, D.E. Milkie, M.W. Davidson, J.A. Galbraith, C.G. Galbraith, and E. Betzig. 2011. Rapid three-dimensional isotropic imaging of living cells using Bessel beam plane illumination. *Nat Methods.* 8:417–423. doi:10.1038/nmeth.1586.
- Poumay, Y., and M.F. Ronveaux-Dupal. 1985. Rapid preparative isolation of concentrated low density lipoproteins and of lipoprotein-deficient serum using vertical rotor gradient ultracentrifugation. *J Lipid Res.* 26:1476–1480. doi:10.1016/S0022-2275(20)34253-X.
- Pszenny, V., K. Ehrenman, J.D. Romano, A. Kennard, A. Schultz, D.S. Roos, M.E. Grigg, V.B. Carruthers, and I. Coppens. 2016. A Lipolytic Lecithin:Cholesterol Acyltransferase Secreted by *Toxoplasma* Facilitates Parasite Replication and Egress. *J Biol Chem.* 291:3725–3746. doi:10.1074/jbc.M115.671974.
- Rivera-Cuevas, Y., J. Mayoral, M.D. Cristina, A.-L.E. Lawrence, E.B. Olafsson, R.K. Patel, D. Thornhill, B.S. Waldman, A. Ono, J.Z. Sexton, S. Lourido, L.M. Weiss, and V.B. Carruthers. 2021. *Toxoplasma gondii* exploits the host ESCRT machinery for parasite uptake of host cytosolic proteins. *PLOS Pathog.* 17:e1010138. doi:10.1371/journal.ppat.1010138.
- Romano, J.D., E.J. Hartman, and I. Coppens. 2021. Quantitative Fluorescence Microscopy for Detecting Mammalian Rab Vesicles within the Parasitophorous vacuole (PV) of the Human Pathogen *Toxoplasma gondii*. In *Rab GTPases: Methods and Protocols*. G. Li and N. Segev, editors. Springer US, New York, NY. 295–305.
- Romano, J.D., S.J. Nolan, C. Porter, K. Ehrenman, E.J. Hartman, R. Hsia, and I. Coppens. 2017. The parasite *Toxoplasma* sequesters diverse Rab host vesicles within an intravacuolar network. *J Cell Biol.* 216:4235–4254. doi:10.1083/jcb.201701108.
- Roos, D.S., R.G. Donald, N.S. Morrisette, and A.L. Moulton. 1994. Molecular tools for genetic dissection of the protozoan parasite *Toxoplasma gondii*. *Methods Cell Biol.* 45:27–63. doi:10.1016/s0091-679x(08)61845-2.
- Schöneberg, J., I.-H. Lee, J.H. Iwasa, and J.H. Hurley. 2017. Reverse-topology membrane scission by the ESCRT complexes. *Nat Rev Mol Cell Biol.* 18:5–17. doi:10.1038/nrm.2016.121.
- von Schwedler, U.K., M. Stuchell, B. Müller, D.M. Ward, H.-Y. Chung, E. Morita, H.E. Wang, T. Davis, G.-P. He, D.M. Cimbara, A. Scott, H.-G. Kräusslich, J. Kaplan, S.G. Morham, and W.I. Sundquist. 2003. The Protein Network of HIV Budding. *Cell.* 114:701–713. doi:10.1016/S0092-8674(03)00714-1.
- Sibley, L.D., I.R. Niesman, S.F. Parmley, and M.F. Cesbron-Delauw. 1995. Regulated secretion of multi-lamellar vesicles leads to formation of a tubulo-vesicular network in host-cell vacuoles occupied by *Toxoplasma gondii*. *J Cell Sci.* 108:1669–1677. doi:10.1242/jcs.108.4.1669.

- Sinai, A.P., P. Webster, and K.A. Joiner. 1997. Association of host cell endoplasmic reticulum and mitochondria with the *Toxoplasma gondii* parasitophorous vacuole membrane: a high affinity interaction. *J Cell Sci.* 110:2117–2128. doi:10.1242/jcs.110.17.2117.
- de Souza, W., and M. Attias. 2015. New views of the *Toxoplasma gondii* parasitophorous vacuole as revealed by Helium Ion Microscopy (HIM). *J Struct Biol.* 191:76–85. doi:10.1016/j.jsb.2015.05.003.
- Sun, S., X. Zhou, J. Corvera, G.E. Gallick, S.-H. Lin, and J. Kuang. 2015. ALG-2 activates the MVB sorting function of ALIX through relieving its intramolecular interaction. *Cell Discov.* 1:1–19. doi:10.1038/celldisc.2015.18.
- Tang, S., W.M. Henne, P.P. Borbat, N.J. Buchkovich, J.H. Freed, Y. Mao, J.C. Fromme, and S.D. Emr. 2015. Structural basis for activation, assembly and membrane binding of ESCRT-III Snf7 filaments. *eLife.* 4:e12548. doi:10.7554/eLife.12548.
- Teis, D., S. Saksena, and S.D. Emr. 2008. Ordered Assembly of the ESCRT-III Complex on Endosomes Is Required to Sequester Cargo during MVB Formation. *Dev Cell.* 15:578–589. doi:10.1016/j.devcel.2008.08.013.
- Vietri, M., M. Radulovic, and H. Stenmark. 2020. The many functions of ESCRTs. *Nat Rev Mol Cell Biol.* 21:25–42. doi:10.1038/s41580-019-0177-4.
- Yang, B., G. Stjepanovic, Q. Shen, A. Martin, and J.H. Hurley. 2015. Vps4 disassembles an ESCRT-III filament by global unfolding and processive translocation. *Nat Struct Mol Biol.* 22:492–498. doi:10.1038/nsmb.3015.

**Main abbreviations:** ALG-2, apoptosis linked gene 2; ALIX, ALG-2-interacting protein X; CHMP, charged multivesicular body protein; CHMP4B-mEm, CHMP4B tagged with C-terminal mEmerald; DN, dominant negative; ESCRT, endosomal sorting complex required for transport; IFA, immunofluorescence assay; IVN, intravacuolar network; mEm-CHMP4B, CHMP4B tagged with N-terminal mEmerald; p.i., post-infection; PV, parasitophorous vacuole; PVM, PV membrane; TgGRA, *Toxoplasma* dense granule protein; TSG101, tumor susceptibility gene 101 protein, WT, wild-type; +PDM, positive product of the difference of the means; MCC, Mander’s colocalization coefficient.



# Figures

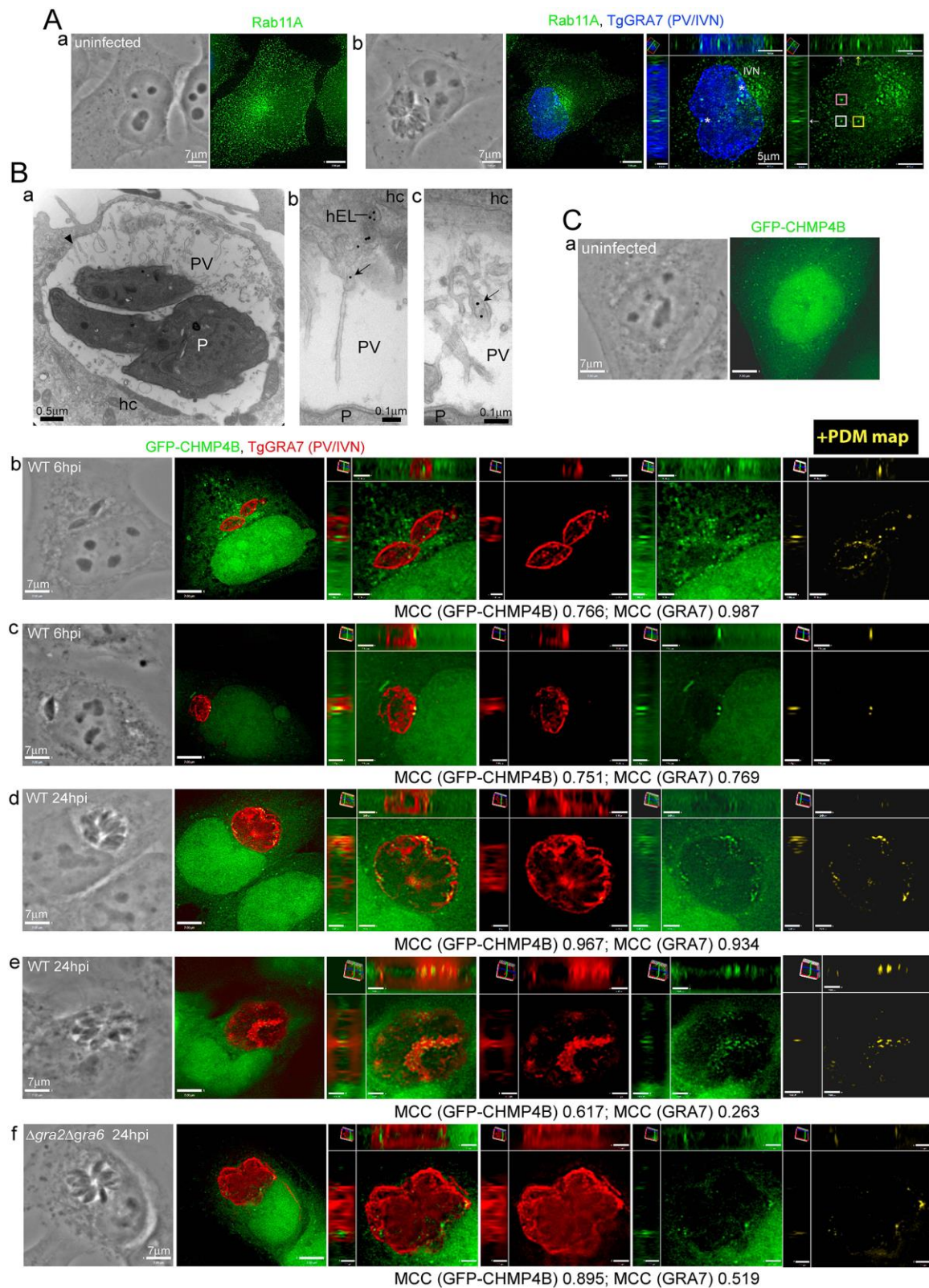


**Fig. 1. Localization of CHMP4B and Rab11A in infected cells.** (A) IFA. Uninfected and infected (20 h) HeLa were fixed and immunostained for Rab11A and TgGRA7. Individual z-slices and cropped images of the PV (orthogonal views) shown. Intra-PV Rab11A puncta are shown in squares. Asterisks show patches of IVN. (B) EM. Infected VERO were incubated with LDL-gold particles for 24 h before fixation. Arrowhead shows an IVN tubule attached to the PVM. hc, host cell; hEL, host endo-lysosome; P, parasite. (C) IFA. Uninfected (a) and HeLa stably expressing GFP-CHMP4B infected for 6 (b-c) or 24 h (d-f) with WT (b-e) or  $\Delta gra2\Delta gra6$  (f) were immunostained for TgGRA7. A positive product of the difference from the mean (PDM) image is shown, highlighting in yellow the voxels where the intensity values of GFP-CHMP4B and TgGRA7 are above their respective means (overlapping signal). Both PDM images and MCC were thresholded for background, as described in Materials and Methods. Individual z-slices and cropped images of the PV (orthogonal views) shown.

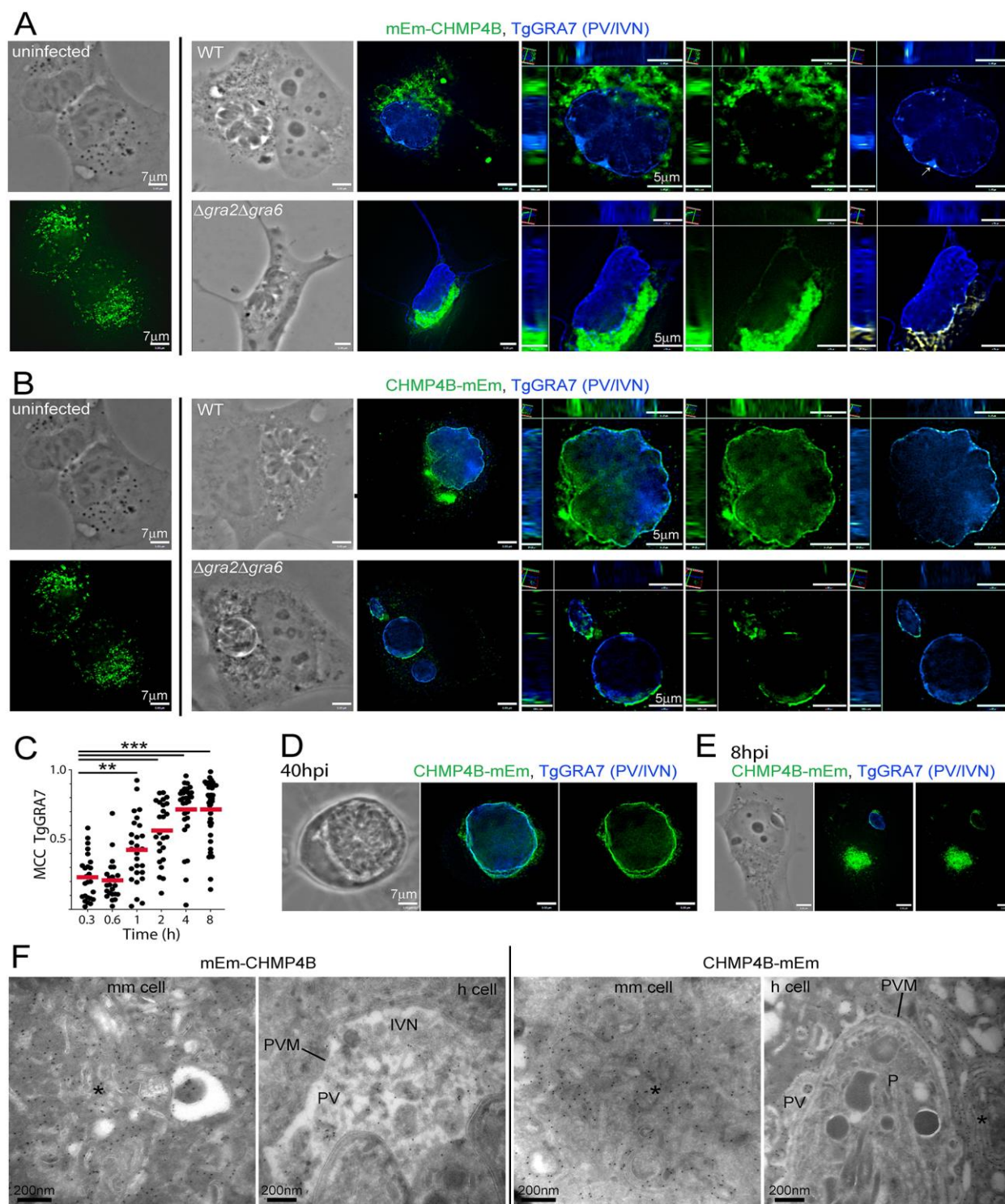


**Fig. 2. Differential PV localization of CHMP4B tagged with either N- or C-terminally mEmerald.** (A-B) IFA. HeLa were transiently transfected with mEm-CHMP4B (A) or CHMP4B-mEm (B). Uninfected and cells infected WT or  $\Delta gra2\Delta gra6$  for 20 h were fixed and immunostained for TgGRA7.

Arrow in A shows CHMP4B staining on the IVN. Individual z-slices and cropped images of the PV (orthogonal views) shown plus positive PDM images. (C) IFA. HeLa transiently transfected with CHMP4B-mEm were infected with WT parasites at the indicated times, fixed and immunostained for TgGRA7. Mander's correlation coefficients (MCC, TgGRA7) were calculated with Volocity. Dot blots are shown with red bars indicating the mean. Number of PV measured (0.3 h, 25; 0.6 h, 23; 1 h, 27; 2 h, 25; 4 h, 30; 8 h, 40) from one representative experiment. p-values, \*\*\*<0.0001, \*\*=0.0098. One-way ANOVA with Tukey multiple comparisons. (D-E) IFA. HeLa transiently transfected with CHMP4B-mEm were infected with WT parasites for 40 (D) or 8 h (E), fixed and immunostained for TgGRA7. Individual z-slices shown. (F-G) ImmunoEM. HeLa transiently transfected with either mEm-CHMP4B (F) or CHMP4B-mEm (G) and either uninfected (left panels) or infected with WT parasites for 20 h. Asterisks show "Class E"-like compartments. mm cell, mammalian cell; h cell, host cell; P, parasite.



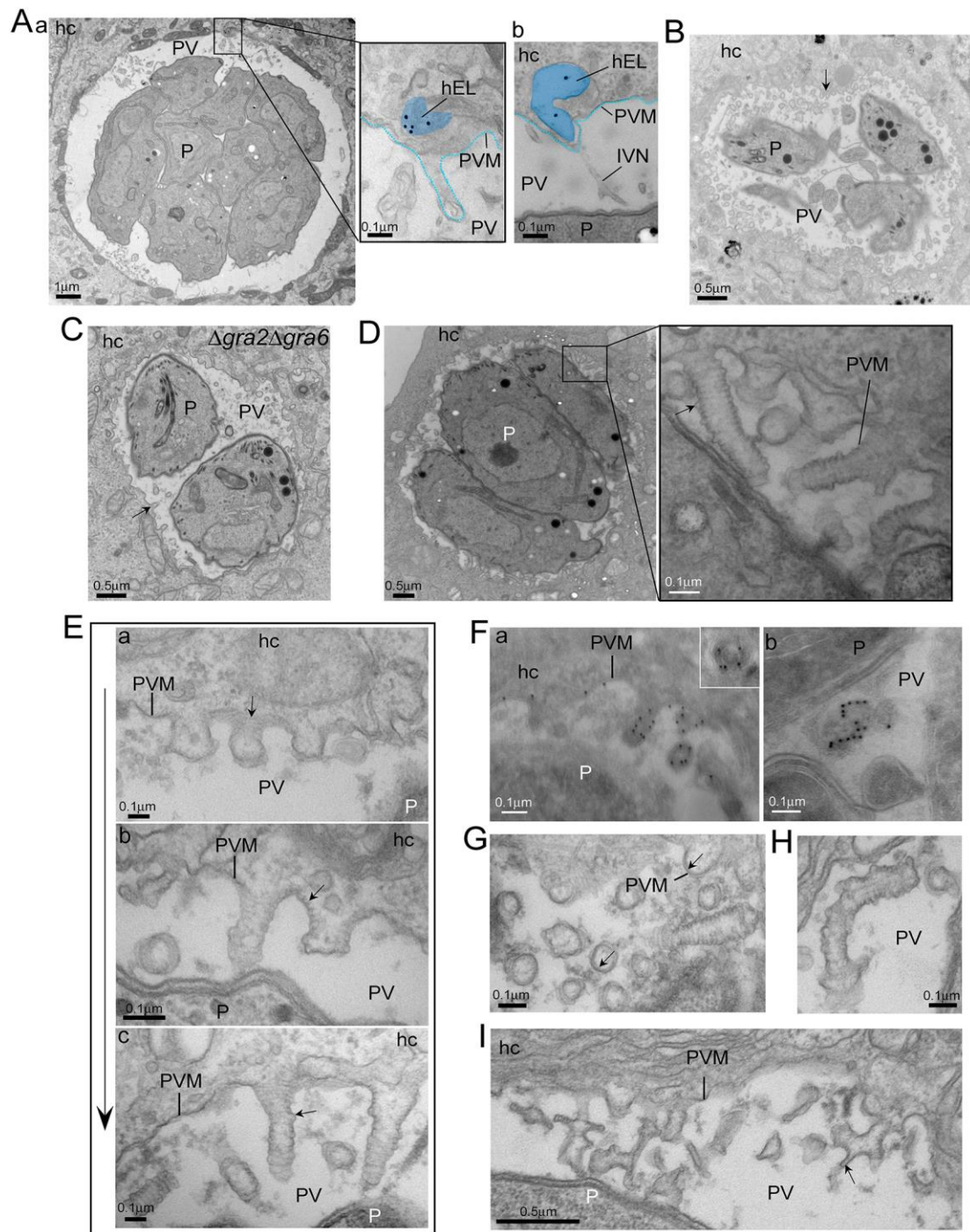


**Fig. 3. Ultrastructure of PV in HeLa cells expressing CHMP4B-mEmerald.** (A-I) EM. (A) Infected HeLa were incubated with LDL-gold particles for 20 h to track host endo-lysosomes (hEL, pseudocolored in blue; inset, panels a and b). (B-C) HeLa transfected with CHMP4B-mEm and infected (B) showing extensive PVM remodeling or with  $\Delta gra2\Delta gra6$  parasites (C) showing fewer and smaller tubules at the PVM. Arrows show PVM buds or tubules. (D-I) Infected CHMP4B-mEm-expressing HeLa detailing

numerous large tubular structures showing regular constrictions (arrow in D). In E, panels a-c show examples of different PVM tubule lengths (arrows). In F, immunogold staining with anti-GFP antibody showing gold particles within tubules. In G, transversal sections of tubules showing CHMP4B filaments inside tubules (arrows) identifiable by their higher electron-density compared to tubular membrane. In H and I, illustration of curled or ramified tubules. Arrow (I) shows a smaller tubule, likely from the IVN, attached to a large, constricted tubule. hc, host cell; P, parasite.



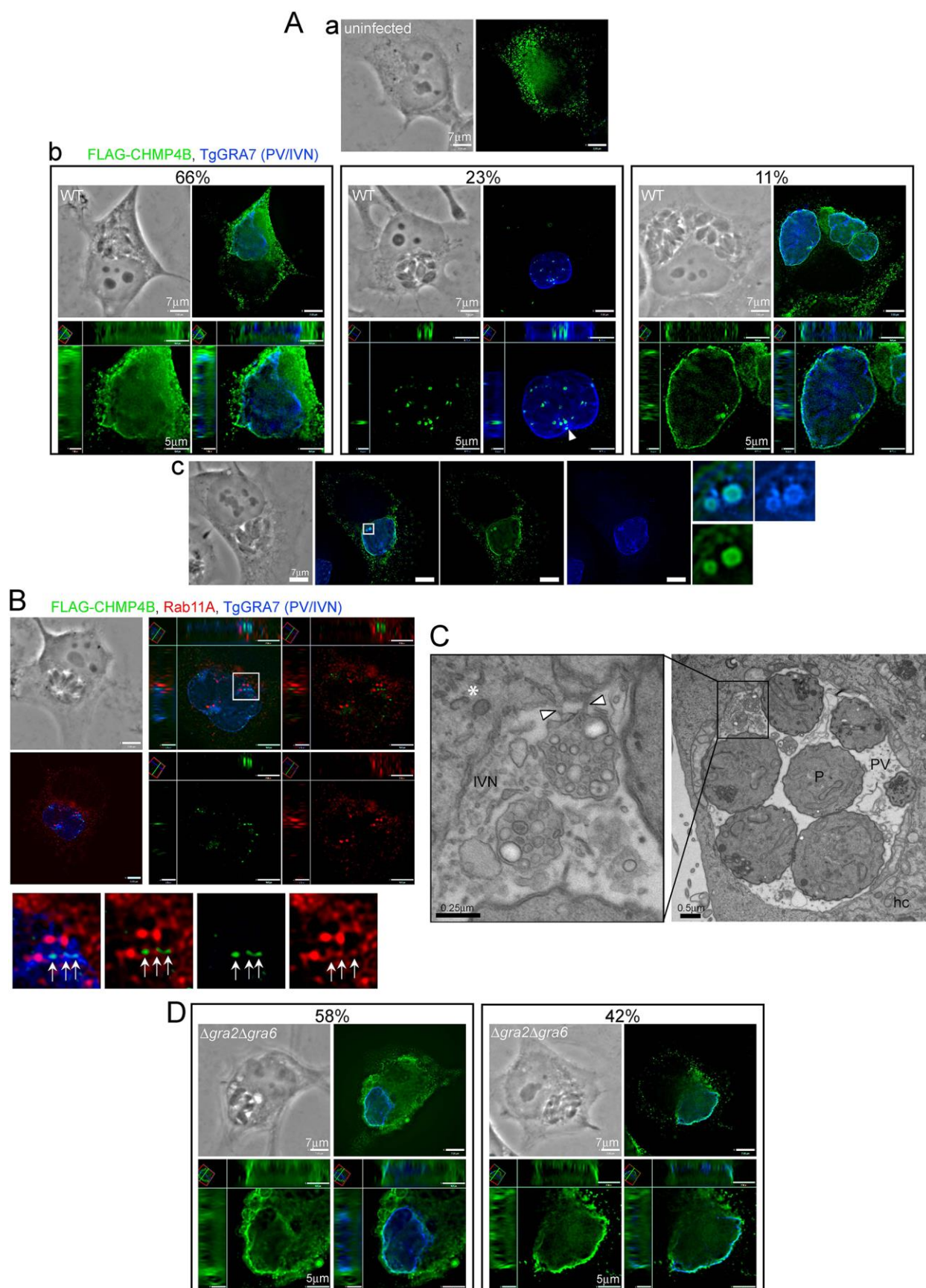


**Fig. 4. Association of FLAG-CHMP4B with the PV.** (A) IFA. HeLa were transiently transfected with FLAG-CHMP4B and either uninfected (panel a) or infected (panels b and c) for 20 h, fixed and immunostained for FLAG and TgGRA7. Percent of infected cells with the displayed morphology shown. (B) IFA. HeLa transiently transfected with FLAG-CHMP4B were infected for 20 h, fixed and immunostained for FLAG, Rab11A and TgGRA7. (A-B) Individual z-slices and cropped images of the PV (orthogonal views) shown plus positive PDM images (yellow). Enlarged regions show overlap of FLAG-CHMP4B and Rab11A puncta (arrows). (C) EM. Infected HeLa expressing FLAG-CHMP4B showing accumulation of large intra-PV multi-vesicular structures, some with a visible connection with the PVM (arrowheads). hc, host cell; P, parasite. (D) HeLa cells expressing FLAG-CHMP4B infected with  $\Delta gra2\Delta gra6$  parasites as in (A).

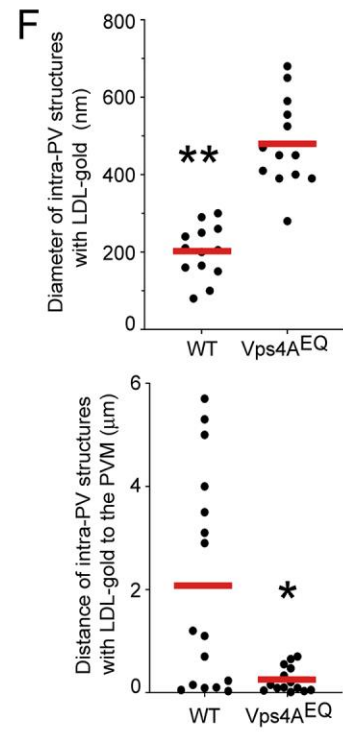
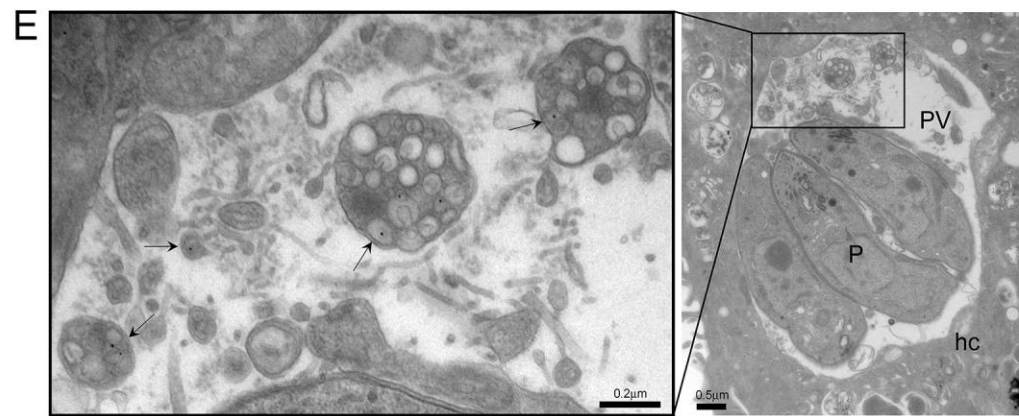
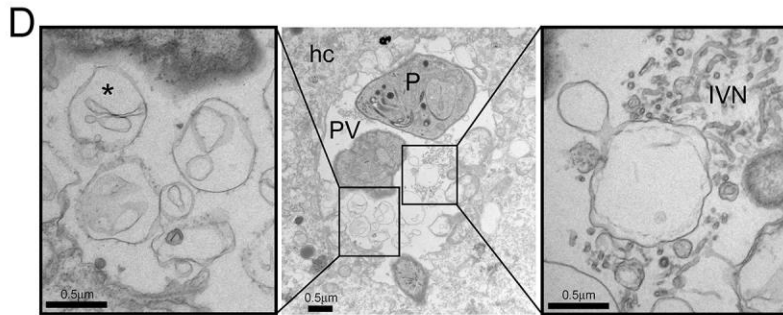
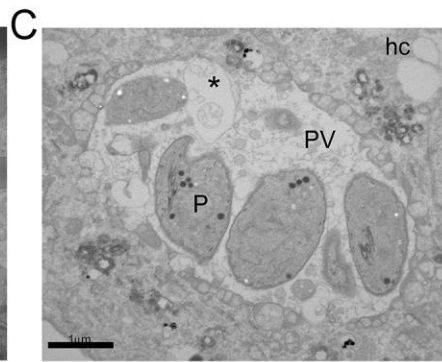
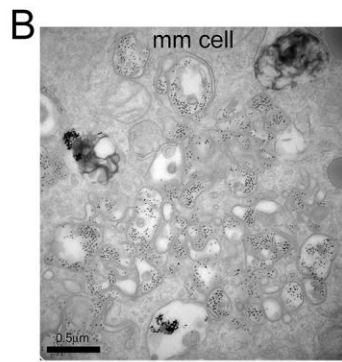
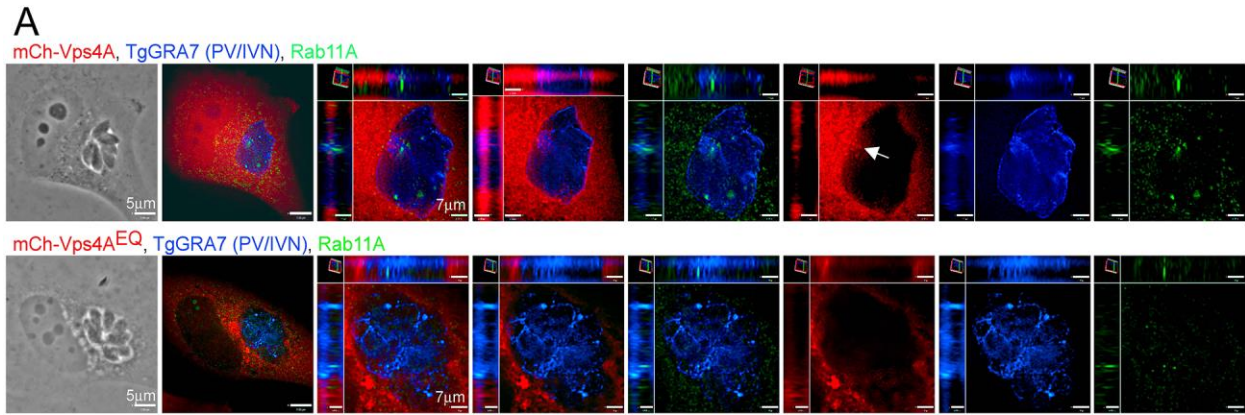


**Fig. 5. Effect of DN Vps4 on host organelle internalization.** (A) IFA. HeLa were transiently transfected with either mCherry-Vps4A<sup>WT</sup> or -Vps4A<sup>EQ</sup>. The cells were infected for 20 h, fixed and immunostained for TgGRA7 and Rab11A. Individual z-slices and cropped images of the PV (orthogonal views) shown. Arrow indicates PV-associated mCherry-Vps4A. (B-F) EM. Infected HeLa expressing mCherry-Vps4A<sup>EQ</sup> and incubated with LDL-gold particles showing class E-like compartments containing gold particles in the host cytoplasm (B) and large membrane buds derived from the PVM (C, D; asterisks), some in contact with IVN tubules shown in D (right inset). In E, intra-PV detection of very large structures with host LDL-gold organelles accumulated (arrows) hc, host cell; P, parasite. (F) Measurement of the size and distance of intra-PV structures containing LDL-gold from their center to the PVM. Dot blots shown with red bars indicating the mean from one representative experiment. For p-values (unpaired, two-tailed t test), \*\*p<0.0001, \*p=0.0032. Intra-PV host organelles size and distance performed on 19 to 23 representative PV sections.



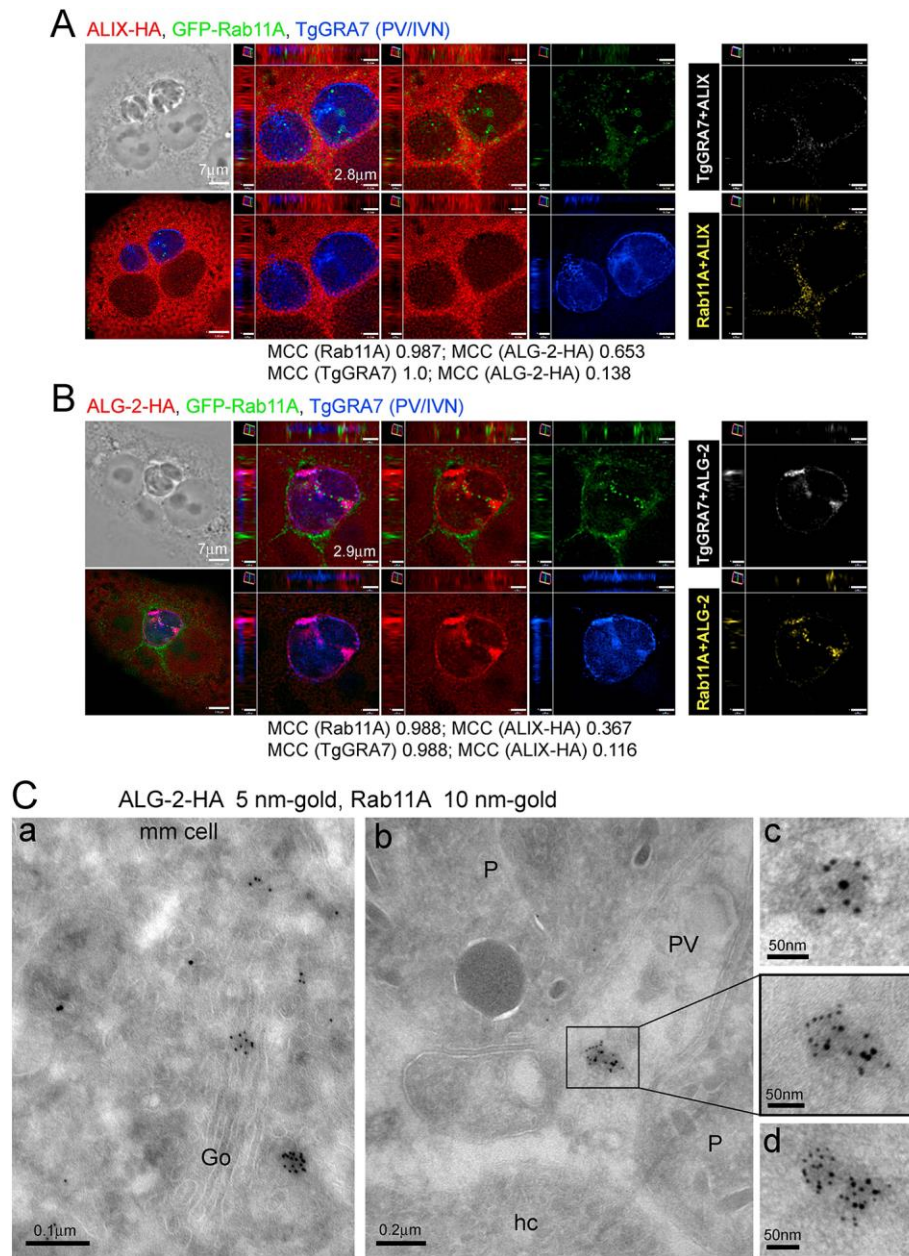


**Fig. 6. Association of mammalian ALIX and ALG-2 with intra-PV Rab11A vesicles.** (A-B). IFA. VERO stably expressing GFP-Rab11A were transfected with ALIX-HA (A) or ALG-2-HA (B), infected for 20 h, fixed and immunostained for HA and TgGRA7. Individual z-slices and cropped images of the PV (orthogonal views) shown. Boxed regions are shown in enlargements and arrows indicate overlap of GFP-Rab11A and ALIX-HA (A). In A, positive PDM images correlating ALIX-HA with GFP-Rab11A (yellow) and the PVM (GRA7) (white) and in B, positive PDM images correlating ALG-2-HA with GFP-Rab11A (yellow) or TgGRA7 (white) are shown. (C) ImmunoEM. HeLa transfected with ALG-2-HA, infected for 20 h and fixed and processed for immunoEM with anti-HA (5 nm-gold) and anti-Rab11A (10

nm-gold) antibodies. (a) ALG-HA and Rab11A in the mammalian cell (b) intra-PV structure with Rab11A membranes surrounded by ALG-2-HA (boxed region, with enlargement). (c, d) Additional illustrations of intra-PV Rab11A vesicles surrounded by ALG-2-HA containing membranes. mm, mammalian cell; Go, Golgi; P, parasite; hc, host cell.



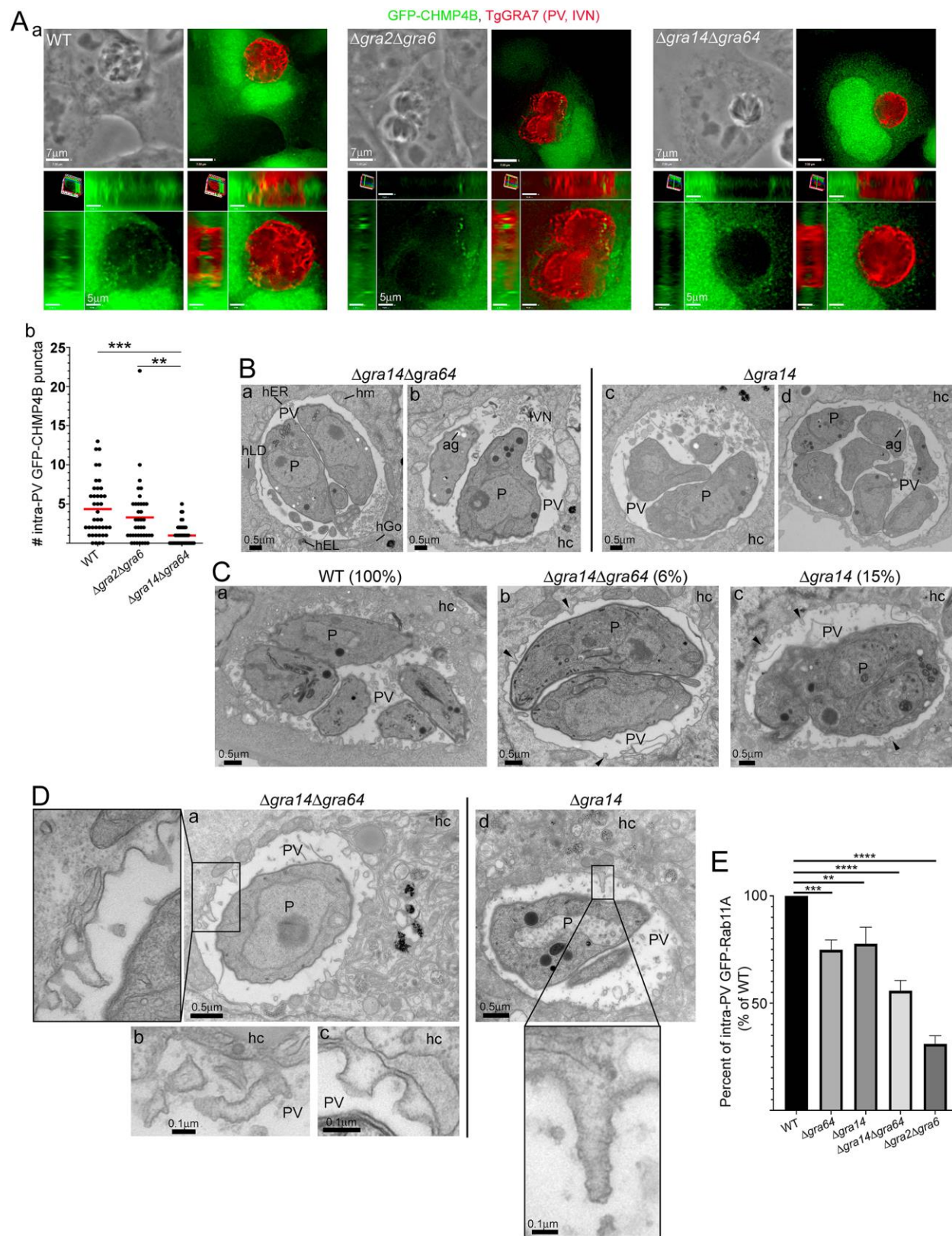


**Fig. 7. Defects in  $\Delta gra14$ ,  $\Delta gra64$  and  $\Delta gra14\Delta gra64$  parasites in PVM remodeling and Rab11A vesicle internalization.** (A) IFA. HeLa stably expressing GFP-CHMP4B were infected with WT,  $\Delta gra2\Delta gra6$  or  $\Delta gra14\Delta gra64$  parasites for 20 h, fixed and immunostained for TgGRA7. (a) Individual z-slices and cropped images of the PV (orthogonal views). (b) The number of intra-PV GFP-CHMP4B puncta was measured for each mutant as described in Materials and Methods. Dot plot from a representative experiment with mean (red bar) shown. Number of PV measured: WT (40),  $\Delta gra2\Delta gra6$  (39),  $\Delta gra14\Delta gra64$  (49). p-values,  $**=0.002$ ,  $****<0.0001$ . One-way ANOVA with Tukey multiple comparisons. (B-D) EM. HeLa non-transfected (B) or transfected with CHMP4B-mEm (C, D) were infected with WT,  $\Delta gra14\Delta gra64$  or  $\Delta gra14\Delta gra64$  parasites for 20 h and incubated with LDL-gold for ultrastructural analysis. In panel D, the arrowhead points to short striated buds from the PVM of the mutants. Percent numbers represent the PV sections in which striated buds/invaginations were observed divided by total sections examined (66 for WT; 39 for  $\Delta gra14$  and 47 for  $\Delta gra14\Delta gra64$  parasites). ag, amylopectin granule; hc, host cell; hEL, host endo-lysosome; hGo, host Golgi; hLD, host lipid droplet; hm, host mitochondrion; P, parasite. (E) VERO stably expressing GFP-Rab11A were infected with WT or indicated knockout mutant parasites for 20 h, fixed and immunostained with TgGRA7. The number of intra-PV Rab11A puncta were measured using Volocity. The mean number of intra-PV GFP-Rab11A puncta was calculated for each sample per experiment and converted into percent of WT. Then, the mean  $\pm$ SD was calculated for the 3 experiments and plotted. Mean values  $\pm$  SD,  $n = 3$  independent experiments, percent of WT is shown. Number of PV measured per experiment: WT (25, 26, 30);  $\Delta gra64$  (28, 22, 25);  $\Delta gra14$  (28, 25, 32);  $\Delta gra14\Delta gra64$  (24, 26, 30);  $\Delta gra2\Delta gra6$  (34, 26, 27). p-values,  $**=0.0015$ ,  $***=0.0006$ ,  $****<0.0001$ . One-way ANOVA with Tukey multiple comparisons.

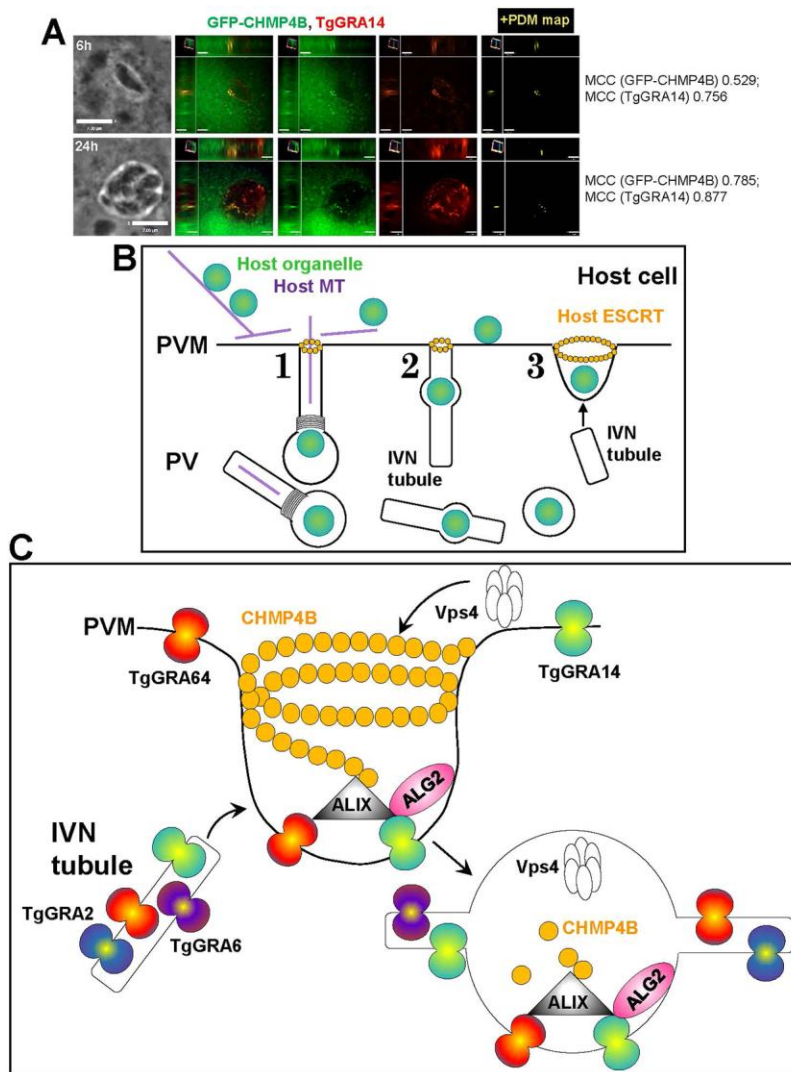


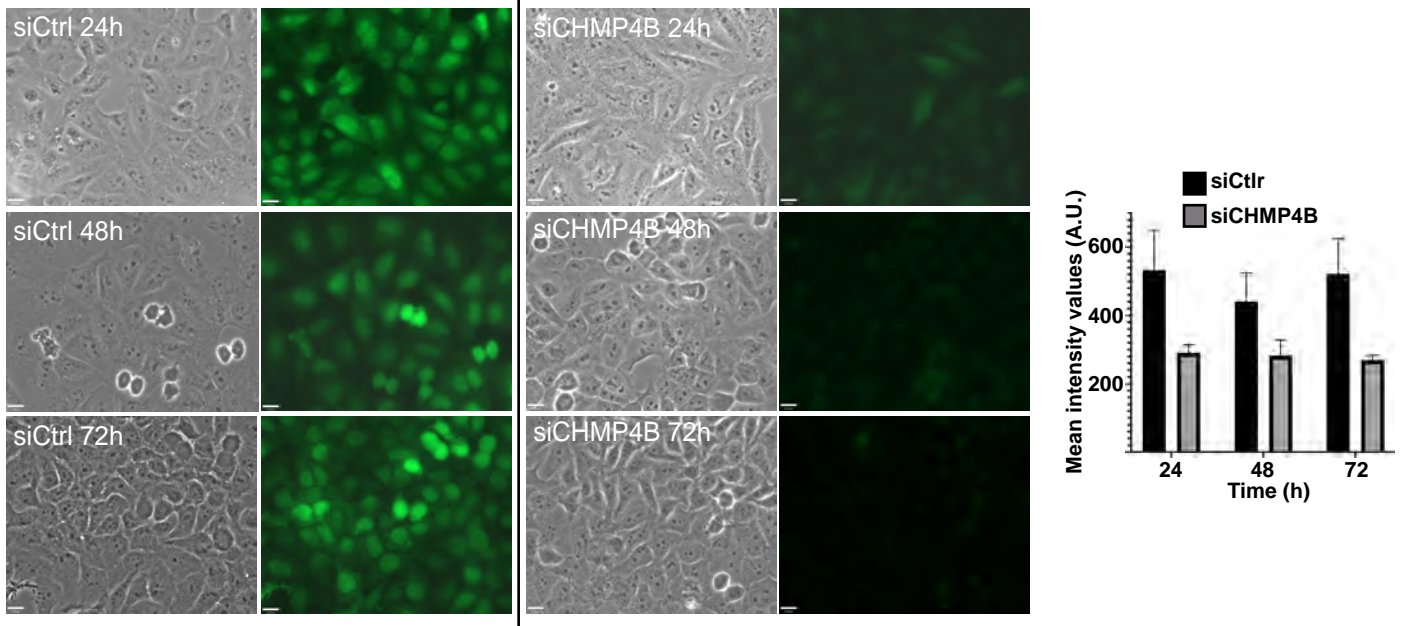
**Fig. 8. TgGRA14 colocalization with GFP-CHMP4B and prospective model of host ESCRT-III components and Vps4 at the PV for internalization of host organelle in synergy with the IVN.** (A) IFA. HeLa stably expressing GFP-CHMP4B were infected for 6 or 24 h and immunostained for TgGRA7. Individual z-slices and cropped images of the PV (orthogonal views) are shown plus positive PDM images (yellow). (B) Overview of cellular events leading to host organelle trafficking along microtubules and internalization into the PV. Three PVM invaginations are depicted: 1. Host microtubule-based invagination; 2. IVN tubule fused with the PVM; 3. Bud with broad neck. Host ESCRT-III components are recruited at the neck of these invaginations for detachment from the PVM. (C) Molecular players involved host organelle internalization (host organelles not shown for clarity). TgGRA14 and TgGRA64 at the PV bind to ALIX interacting with CHMP4B subunits that cluster, resulting in deep membrane concavities with the walls of the membrane neck close enough for fusion

prior to Vps4 scission activity. Concomitant, IVN tubules fuse with CHMP4B-induced tubules, contributing to their elongation and supply in TgGRA14 and TgGRA64. Upon PVM detachment, tubulo-vesicles derived with PVM and IVN containing host organelles and residual ESCRT-III components/Vps4, accumulate inside the PV.

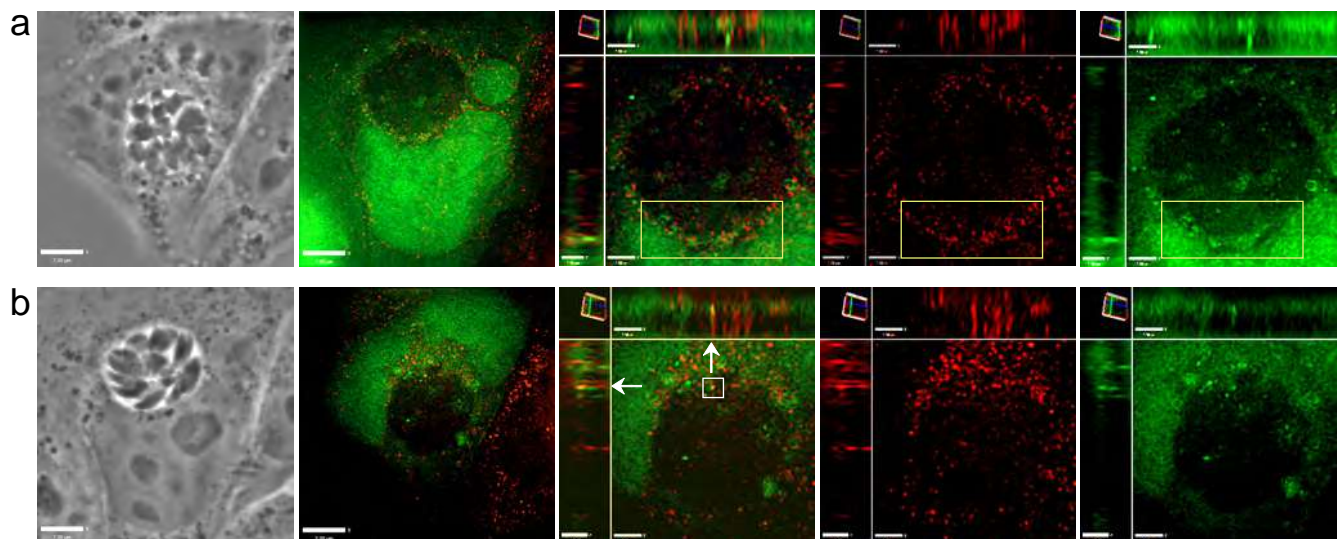


Figure S1

## A GFP-CHAMP4B



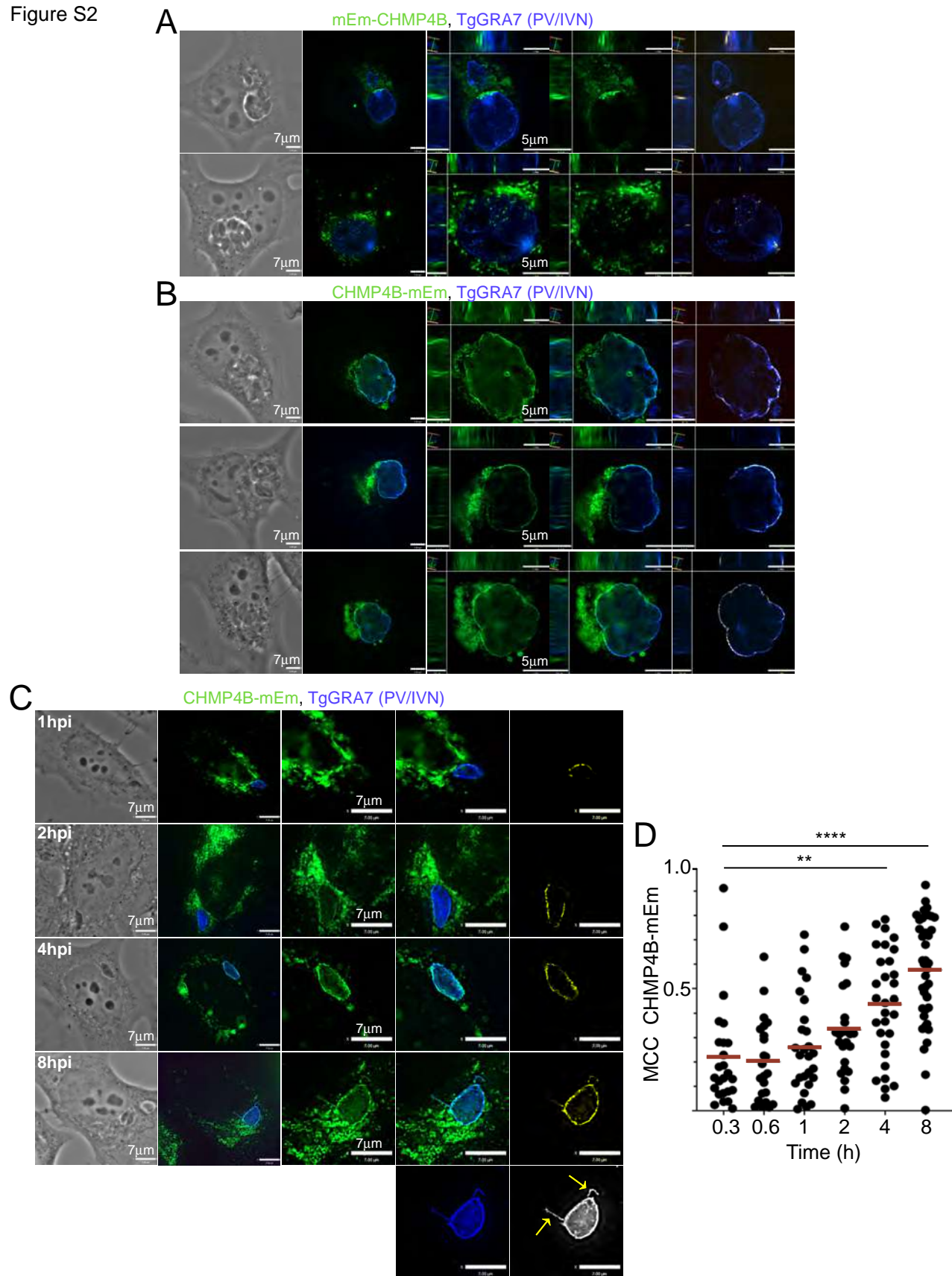
## B GFP-CHAMP4B, Rab11A



**Fig. S1. GFP-CHMP4B silencing and relative localization to Rab11A.** (A) Fluorescence microscopy. Silencing of GFP-CHMP4B showing representative fields of HeLa stably expressing GFP-CHMP4B transfected with control or CHMP4B siRNA for 24, 48, or 72 h. Mean fluorescence intensity of GFP-CHMP4B was measured as described in Materials and Methods. Mean of 15 random fields with SD are shown from one representative experiment. (B) IFA. HeLa stably expressing GFP-CHMP4B and infected for 24 h were fixed and immunostained for Rab11A. Individual z-slices and cropped images of the PV (orthogonal views) shown. Box in panel a shows GFP-CHMP4B and Rab11A accumulating along the PV while arrows in panel b show overlap of a GFP-CHMP4B and Rab11A puncta.

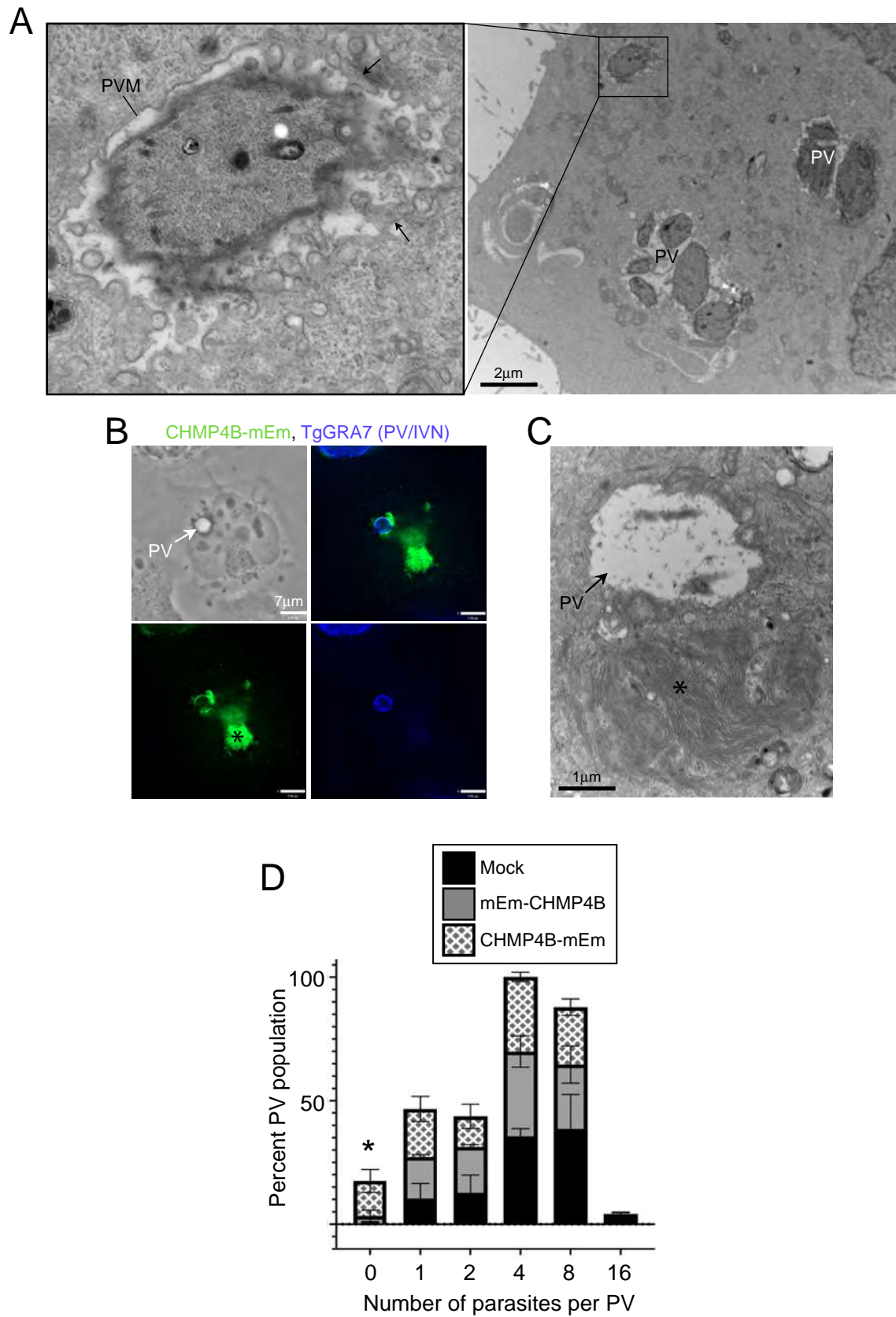


Figure S2



**Fig. S2. Differential PV localization of mEmerald-CHMP4B and CHMP4B-mEmerald.** (A-B) IFA. HeLa were transiently transfected with either mEm-CHMP4B (A) or CHMP4B-mEm (B), infected for 20 h, fixed and immunostained for TgGRA7. Individual z-slices and cropped images of the PV (orthogonal views) shown. A positive PDM image is shown, highlighting in yellow of voxels where both CHMP4B and TgGRA7 intensity values were above their respective means. (C) IFA. HeLa transiently transfected with CHMP4B-mEm were infected at the indicated times, fixed and immunostained for TgGRA7. A positive PDM image is shown (yellow). Arrows show PVMP containing CHMP4B. (D) HeLa transiently transfected with CHMP4B-mEm were infected, fixed and immunostained for TgGRA7. Mander's correlation coefficients (MCC, CHMP4B-mEm) were calculated with Volocity. Dot plots are shown with red bars indicating the mean from one representative experiment. Number PV measured per time point: 0.3 h, 25; 0.6 h, 23; 1 h, 27; 2 h, 25; 4 h, 30; 8 h, 40. p-values, \*\*\*\*<0.0001, \*\*=0.0019. One-way ANOVA with Tukey multiple comparisons.

Figure S3

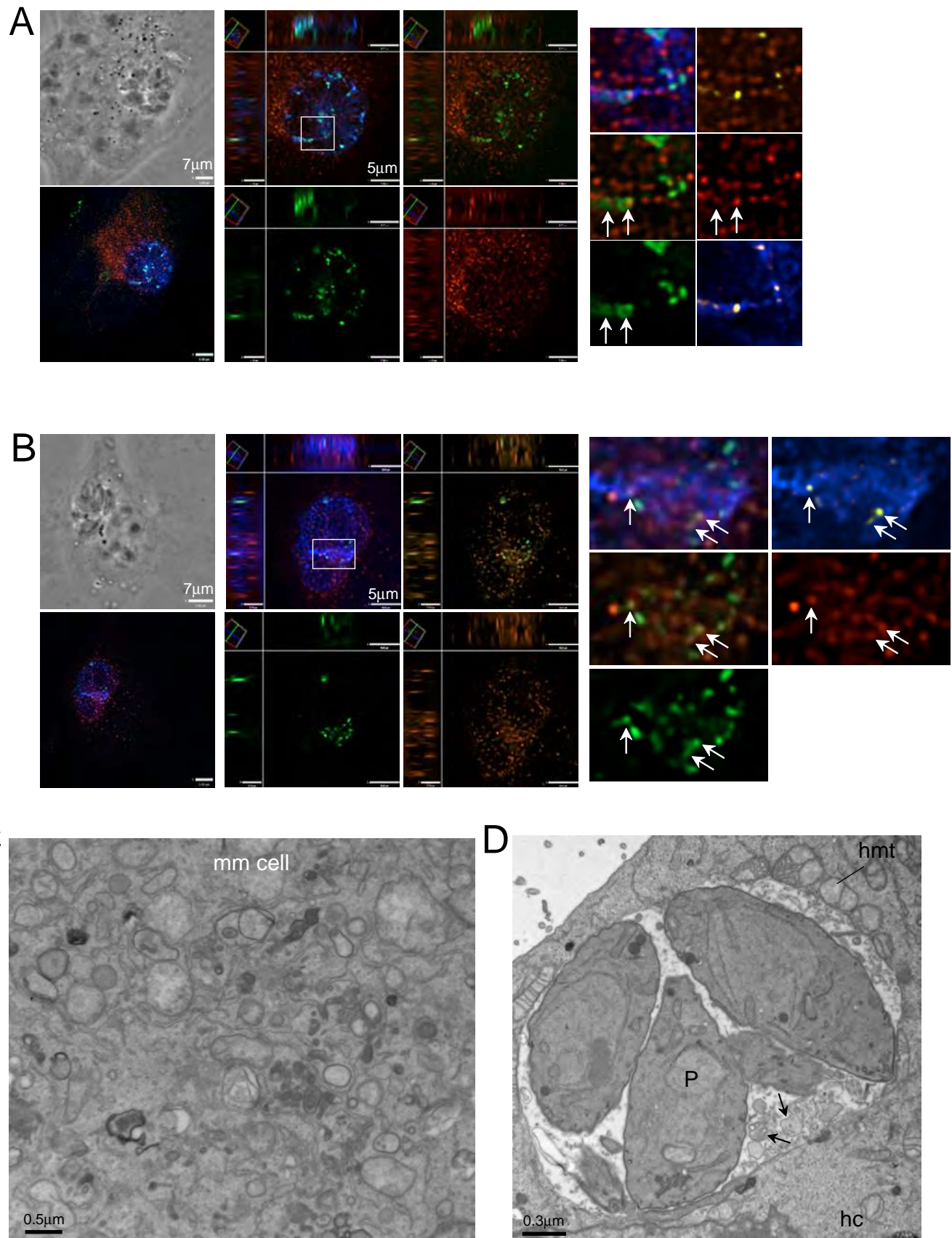


**Fig. S3. Defective PV in cells expressing CHMP4B-mEmerald.** (A) EM. HeLa transfected with CHMP4B-mEm and infected for 20 h, showing PV with disorganized parasites in PV, almost no host ER and mitochondria associated with the PVM and many small PV with numerous PVM indentations. (B) IFA. HeLa transfected with CHMP4B-mEm were infected with WT parasites for 20 h, fixed and immunostained with anti-GFP and TgGRA7 antibodies. Asterisk shows ‘class E-like’ compartments and arrow a PV devoid of parasite. (C) EM. HeLa transfected with CHMP4B-mEm and infected with WT parasites for 20 h, showing an “empty” PV reminiscent of the IFA image in B. (D) Enumeration of parasites within each PV in HeLa cells either mock-transfected or transfected with either mEm-CHMP4B or CHMP4B-mEm and infected for 20 h. Number of parasites equaling zero corresponds to empty PV as in (B). Means  $\pm$  SD,  $n=3$  independent experiments. PV were defined as positive for TgGRA7 staining. Number of PV counted per condition: mock (236, 343, 270); mEm-CHMP4B (189, 294, 191); CHMP4B-mEm (166, 299, 226) p-values,  $p=0.0030$  (Mock vs. C-tag, 0/PV);  $p=0.0095$  (N-tag vs. C-tag, 0/PV). One-way ANOVA with Tukey multiple comparisons.



Figure S4

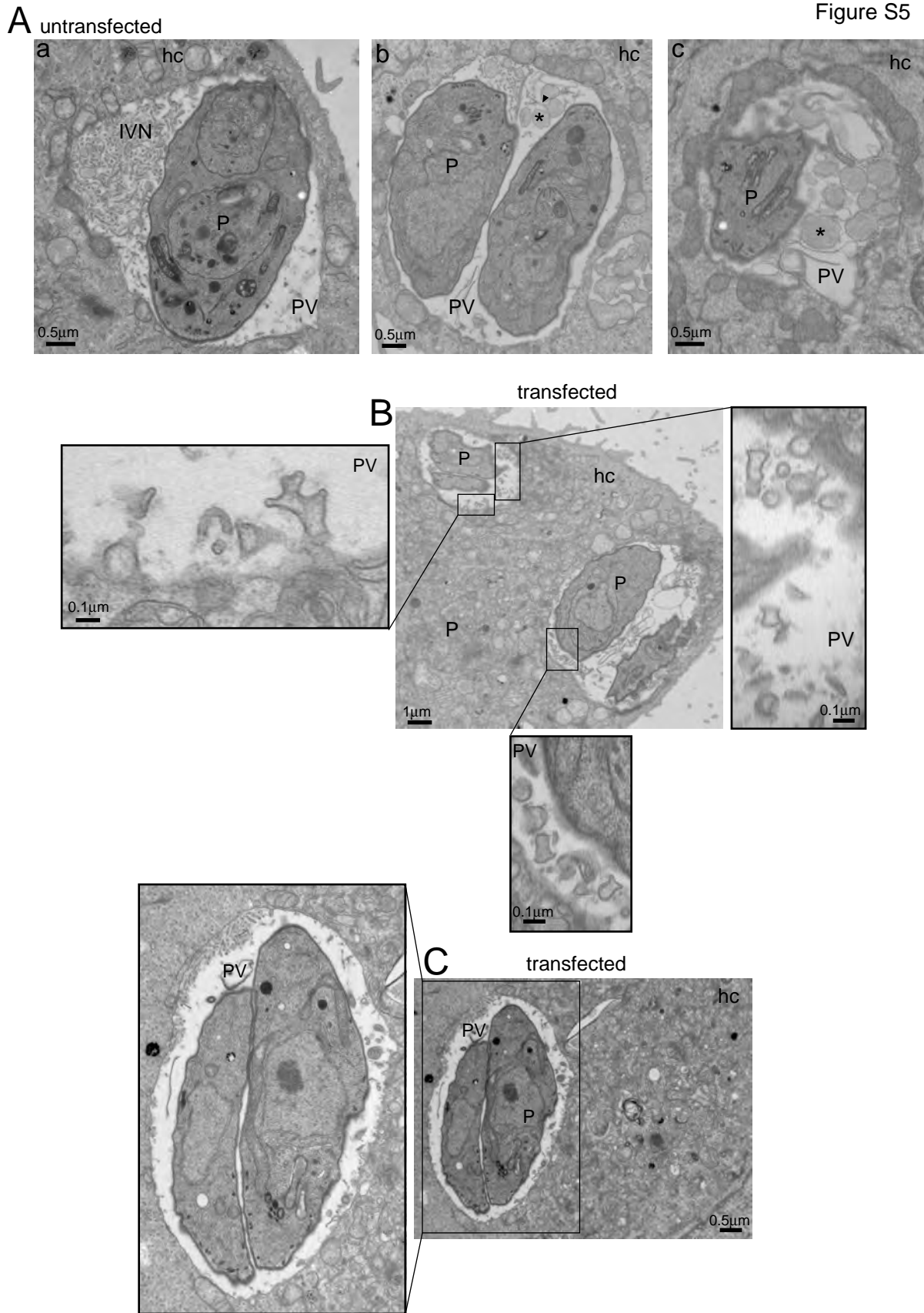
FLAG-CHMP4B, Rab11A, TgGRA7 (PV/IVN)



**Fig. S4. Distribution of intra-PV FLAG-CHMP4B and Rab11A puncta.** (A-B) IFA. HeLa transiently transfected with FLAG-CHMP4B and infected for 20 h were fixed and immunostained for FLAG, Rab11A and TgGRA7. Individual z-slices and cropped images of the PV (orthogonal views) are shown. Many FLAG-CHMP4B puncta associated with the PV (TgGRA7) and some puncta overlap with Rab11A (enlargements, arrows). (C-D) EM. Infected HeLa expressing FLAG-CHMP4B showing accumulation of numerous vesicles in the cytoplasm of host cells (C), no PVM remodeling but accumulation of large intra-PV multivesicular structures (arrows), mm cell, mammalian cell; hc, host cell; hmt, host mitochondria; P, parasite.



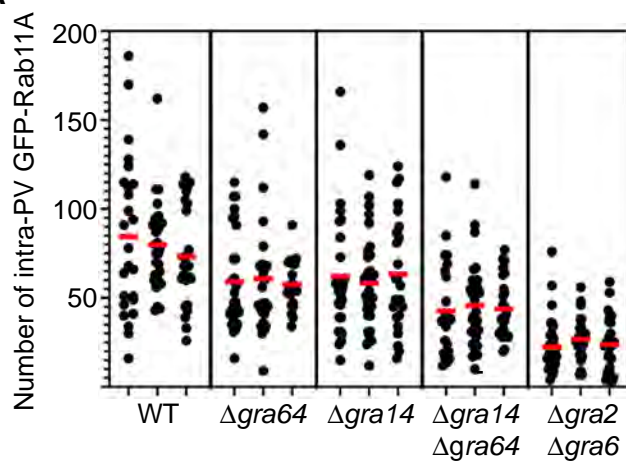
Figure S5



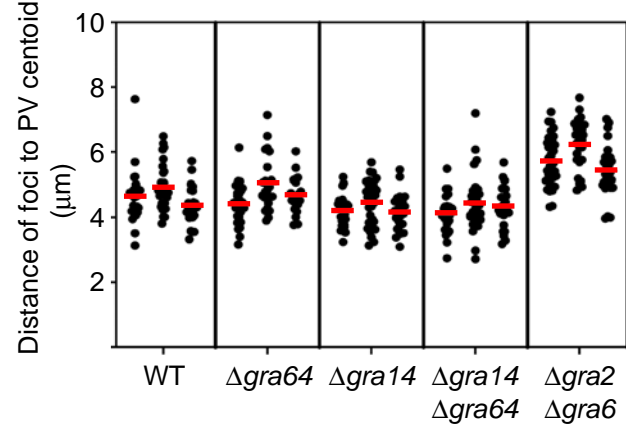
**Fig. S5. Ultrastructure of  $\Delta$ gral4 $\Delta$ gra64 parasites.** (A-C) EM. HeLa non-transfected (A) or transfected with CHMP4B-mEmerald (B, C) were infected with  $\Delta$ gral4 $\Delta$ gra64 parasites for 20 h and incubated with LDL-gold for ultrastructural analysis. Asterisks point to unidentified fibrous structure. hc, host cell.

Figure S6

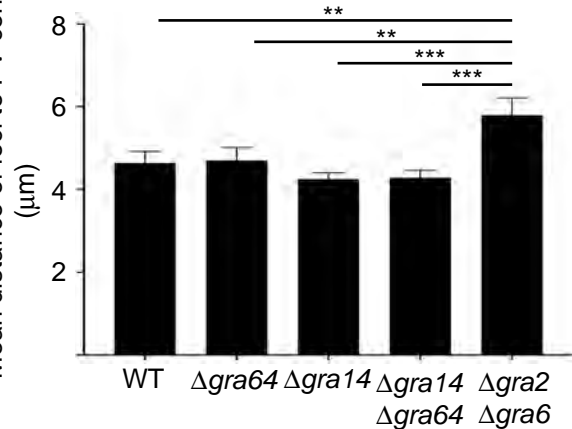
**A**



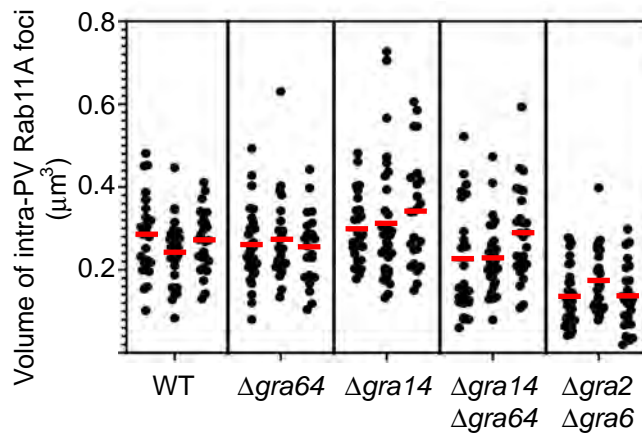
**B**



Mean distance of foci to PV centroid ( $\mu m$ )



**C**



Mean volume of intra-PV Rab11A foci ( $\mu m^3$ )

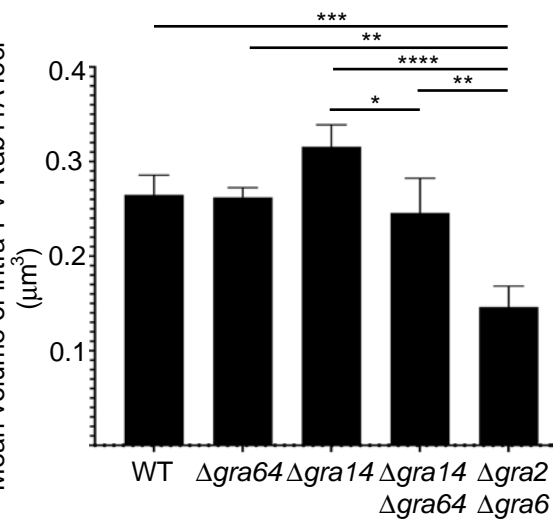


**Fig. S6. Characteristics of intra-PV GFP-Rab11A puncta for WT,  $\Delta gra64$ ,  $\Delta gra14$ ,  $\Delta gra14\Delta gra64$  or  $\Delta gra2\Delta gra6$  parasites.** VERO stably expressing GFP-Rab11A were infected with WT,  $\Delta gra64$ ,  $\Delta gra14$ ,  $\Delta gra14\Delta gra64$  or  $\Delta gra2\Delta gra6$  parasites for 20 h, fixed and immunostained with TgGRA7. The number (A), distance from the PV centroid (B) and volume (C) of intra-PV Rab11A puncta were measured using Volocity. Number of PV measured per experiment: WT (25, 26, 30);  $\Delta gra64$  (28, 22, 25);  $\Delta gra14$  (28, 25, 32);  $\Delta gra14\Delta gra64$  (24, 26, 30);  $\Delta gra2\Delta gra6$  (34, 26, 27). (A) Dot plot showing the number of intra-PV GFP-Rab11A puncta for each PV measured for three independent experiments. Red bar, mean. This is the raw data of the mean numbers shown in Fig. 9 E. (B) Dot plot showing the mean distance of intra-PV GFP-Rab11A puncta from the PV centroid for each PV measured for three independent experiments. Red bar, mean. Graph of the mean distance  $\pm$  SD,  $n = 3$  independent experiments. p-values, \*\*\*  $<0.0005$ , \*\* = 0.0066. (C) Dot plot showing the mean volume of intra-PV GFP-Rab11A puncta for each PV measured for three independent experiments. Red bar, mean. Graph of mean volume  $\pm$  SD.  $n = 3$  independent experiments. p-values, \*\*\*\* $<0.0001$ , \*\*\*=0.0009, \*\*=0.0035, \*=0.033. One-way ANOVA with Tukey multiple comparisons (B, C).